

A stabilized finite element formulation for liquid shells and its application to lipid bilayers

Roger A. Sauer^{*1}, Thang X. Duong^{*}, Kranthi K. Mandadapu^{†§} and David J. Steigmann[‡]

**Aachen Institute for Advanced Study in Computational Engineering Science (AICES),
RWTH Aachen University, Templergraben 55, 52056 Aachen, Germany*

*†Department of Chemical and Biomolecular Engineering, University of California at Berkeley,
110 Gilman Hall, Berkeley, CA 94720-1460, USA*

§Chemical Sciences Division, Lawrence Berkeley National Laboratory, CA 94720, USA

*‡Department of Mechanical Engineering, University of California at Berkeley,
6141 Etcheverry Hall, Berkeley, CA 94720-1740, USA*

Abstract

This paper presents a new finite element (FE) formulation for liquid shells that is based on an explicit, 3D surface discretization using C^1 -continuous finite elements constructed from NURBS interpolation. Both displacement-based and mixed FE formulations are proposed. The latter is needed for area-incompressible material behavior, where penalty-type regularizations can lead to misleading results. In order to obtain quasi-static solutions, several numerical stabilization schemes are proposed based on either stiffness, viscosity or projection. Several numerical examples are considered in order to illustrate the accuracy and the capabilities of the proposed formulation, and to compare the different stabilization schemes. The presented formulation is capable of simulating non-trivial surface shapes associated with tube formation and protein-induced budding of lipid bilayers. In the latter case, the presented formulation yields non-axisymmetric solutions, which have not been observed in previous simulations. It is shown that those non-axisymmetric shapes are preferred over axisymmetric ones.

Keywords: cell budding, cell tethering, Helfrich energy, isogeometric analysis, non-linear finite elements, non-linear shell theory

Contents

1	Introduction	4
2	Summary of thin liquid shell theory	6
2.1	Thin shell kinematics	7
2.2	Quasi-static equilibrium	8
2.3	Constitution	9
2.3.1	Area-compressible lipid bilayer	9
2.3.2	Area-incompressible lipid bilayer	9
2.3.3	Model properties	10
2.4	Weak form	11

¹corresponding author, email: sauer@aices.rwth-aachen.de

3	Liquid shell stabilization	12
3.1	Adding stiffness	12
3.1.1	In-plane shear and bulk stabilization	12
3.1.2	Sole in-plane shear stabilization	12
3.1.3	Relation to physical viscosity	13
3.2	Normal projection	13
3.3	Summary of the stabilization schemes	15
4	FE formulation	15
4.1	FE approximation	15
4.2	Discretized weak form	16
4.3	Area constraint	17
4.4	Solution procedure	17
4.5	Rotational constraints	18
4.6	Normalization	18
5	Numerical examples	18
5.1	Pure bending and stretching of a flat strip	18
5.2	Inflation of a sphere	22
5.3	Drawing of a tube	24
5.4	Cell budding	28
5.4.1	Motivation	28
5.4.2	Computational setup	28
5.4.3	Bud shapes	29
5.4.4	Surface energy	31
5.4.5	Surface tension	32
5.4.6	Effective shear stiffness	33
5.4.7	Influence of the area-compressibility	34
6	Conclusion	36
A	Linearization of $\mathbf{f}_{\text{into}}^e$	37

List of important symbols

$\mathbf{1}$	identity tensor in \mathbb{R}^3
\mathbf{a}_α	co-variant tangent vectors of surface \mathcal{S} at point \mathbf{x} ; $\alpha = 1, 2$
\mathbf{A}_α	co-variant tangent vectors of surface \mathcal{S}_0 at point \mathbf{X} ; $\alpha = 1, 2$
\mathbf{a}^α	contra-variant tangent vectors of surface \mathcal{S} at point \mathbf{x} ; $\alpha = 1, 2$
\mathbf{A}^α	contra-variant tangent vectors of surface \mathcal{S}_0 at point \mathbf{X} ; $\alpha = 1, 2$
$\mathbf{a}_{\alpha,\beta}$	parametric derivative of \mathbf{a}_α w.r.t. ξ^β
$\mathbf{a}_{\alpha;\beta}$	co-variant derivative of \mathbf{a}_α w.r.t. ξ^β
$a_{\alpha\beta}$	co-variant metric tensor components of surface \mathcal{S} at point \mathbf{x}
$A_{\alpha\beta}$	co-variant metric tensor components of surface \mathcal{S}_0 at point \mathbf{X}
\mathbf{a}	class of stabilization methods based on artificial shear viscosity
\mathbf{A}	class of stabilization methods based on artificial shear stiffness
$b_{\alpha\beta}$	co-variant curvature tensor components of surface \mathcal{S} at point \mathbf{x}
$B_{\alpha\beta}$	co-variant curvature tensor components of surface \mathcal{S}_0 at point \mathbf{X}
\mathbf{B}	left surface Cauchy-Green tensor
$c^{\alpha\beta\gamma\delta}$	contra-variant components of the material tangent
\mathbf{C}	right surface Cauchy-Green tensor
γ	surface tension of \mathcal{S}
$\Gamma_{\alpha\beta}^\gamma$	Christoffel symbols of the second kind
da	differential surface element on \mathcal{S}
dA	differential surface element on \mathcal{S}_0
$\delta\dots$	variation of ...
e	index numbering the finite elements; $e = 1, \dots, n_{el}$
ϵ	penalty parameter
\mathbf{f}^e	finite element force vector of element Ω^e
g	expression for the area-incompressibility constraint
G	expression for the weak form
G^e	contribution to G from finite element Ω^e
\mathbf{g}^e	finite element ‘force vector’ of element Ω^e due to constraint g
H	mean curvature of \mathcal{S} at \mathbf{x}
H_0	spontaneous curvature prescribed at \mathbf{x}
I	index numbering the finite element nodes
I_1, I_2	first and second invariants of the surface Cauchy Green tensors
\mathbf{i}	surface identity tensor on \mathcal{S}
\mathbf{I}	surface identity tensor on \mathcal{S}_0
J	surface area change
k	bending modulus
k^*	Gaussian modulus
K	initial in-plane membrane bulk modulus
K_{eff}	effective in-plane membrane bulk modulus
\mathbf{k}^e	finite element tangent matrix associated with \mathbf{f}^e and \mathbf{g}^e
κ	Gaussian curvature of surface \mathcal{S} at \mathbf{x}
κ_1, κ_2	principal curvatures of surface \mathcal{S} at \mathbf{x}
L_I	pressure shape function of finite element node I
λ_1, λ_2	principal surface stretches of \mathcal{S} at \mathbf{x}
m_e	number of pressure nodes of finite element Ω^e

m_ν, m_τ	bending moment components acting at $\mathbf{x} \in \partial\mathcal{S}$
$\bar{m}_\nu, \bar{m}_\tau$	prescribed bending moment components
$M^{\alpha\beta}$	contra-variant bending moment components
μ	initial in-plane membrane shear stiffness
μ_{eff}	effective in-plane membrane shear stiffness
n_{no}	total number of finite element nodes used to discretize \mathcal{S}
n_{el}	total number of finite elements used to discretize \mathcal{S}
n_{mo}	total number of finite element nodes used to discretize pressure q
n_e	number of displacement nodes of finite element Ω^e
$N^{\alpha\beta}$	total, contra-variant, in-plane membrane stress components
N_I	displacement shape function of finite element node I
\mathbf{n}	surface normal of \mathcal{S} at \mathbf{x}
\mathbf{N}	surface normal of \mathcal{S}_0 at \mathbf{X}
\mathbf{N}	array of the shape functions for element Ω^e
ν	in-plane membrane shear viscosity
$\boldsymbol{\nu}$	normal vector on $\partial\mathcal{S}$
ξ^α	convective surface coordinates; $\alpha = 1, 2$
\mathbf{P}	class of stabilization methods based on normal projection; projection matrix
q	Lagrange multiplier associated with area-incompressibility
\mathbf{q}	array of all Lagrange multipliers q_I in the system; $I = 1, \dots, n_{\text{mo}}$
\mathbf{q}_e	array of all Lagrange multipliers q_I for finite element Ω^e ; $I = 1, \dots, m_e$
S^α	contra-variant, out-of-plane shear stress components
\mathcal{S}	current configuration of the surface
\mathcal{S}_0	initial configuration of the surface
$\boldsymbol{\sigma}$	Cauchy stress tensor of the shell
$\sigma^{\alpha\beta}$	stretch related, contra-variant, in-plane membrane stress components
\mathbf{t}	effective traction acting on the boundary $\partial\mathcal{S}$ normal to $\boldsymbol{\nu}$
$\bar{\mathbf{t}}$	prescribed boundary tractions on Neumann boundary $\partial_t\mathcal{S}$
\mathbf{T}	traction acting on the boundary $\partial\mathcal{S}$ normal to $\boldsymbol{\nu}$
\mathbf{T}^α	traction acting on the boundary $\partial\mathcal{S}$ normal to \mathbf{a}^α
\mathcal{V}, \mathcal{Q}	admissible function spaces
φ	deformation map of surface \mathcal{S}
$\bar{\varphi}$	prescribed boundary deformations on boundary $\partial_x\mathcal{S}$
w	hyperelastic stored surface energy density per current surface area
W	hyperelastic stored surface energy density per reference surface area
\mathbf{x}	current position of a surface point on \mathcal{S}
\mathbf{X}	initial position of \mathbf{x} on the reference surface \mathcal{S}_0
\mathbf{x}_I	position vector of finite element node I lying on \mathcal{S}
\mathbf{X}_I	initial position of finite element node I on \mathcal{S}_0
\mathbf{x}	array of all nodal positions \mathbf{x}_I of the discretized surface; $I = 1, \dots, n_{\text{no}}$
\mathbf{x}_e	array of all nodal positions \mathbf{x}_I for finite element Ω^e ; $I = 1, \dots, n_e$
\mathbf{X}_e	array of all nodal positions \mathbf{X}_I for finite element Ω_0^e ; $I = 1, \dots, n_e$
Ω^e	current configuration of finite element e
Ω_0^e	reference configuration of finite element e

1 Introduction

Biological membranes form the boundaries of cells and cell-internal organelles such as the endoplasmic reticulum, the golgi complex, mitochondria and endosomes. Mechanically they are

liquid shells that exhibit fluid-like behavior in-plane and solid-like behavior out-of-plane. They mainly consist of self-assembled lipid bilayers and proteins. At the macroscopic level, these membranes exist in different shapes such as invaginations, buds and cylindrical tubes (Zimmerberg and Kozlov, 2006; Shibata et al., 2009; McMahon and Gallop, 2005; Shemesh et al., 2014). These shapes arise as a result of the lateral loading due to cytoskeletal filaments and protein-driven spontaneous curvature. Cell membranes undergo many morphological and topological shape transitions to enable important biological processes such as endocytosis (Buser and Drubin, 2013; Kukulski et al., 2012; Peter et al., 2004), cell motility (Keren, 2011) and vesicle formation (Gruenberg and Stenmark, 2004; Budin et al., 2009). The shape transitions occur as a result of lateral loading on the membranes from cytoskeletal filaments, such as actin, from osmotic pressure gradients across the membrane, or from membrane-protein interactions. For example, in endocytosis – a primary mode of transport of cargo between the exterior of the cell and its interior – proteins bind to the flat membrane and induce invaginations or bud shapes, followed by a tube formation by actin-mediated pulling forces (Kukulski et al., 2012; Walani et al., 2015).

Most of the computational studies regarding biological membranes are restricted to shapes resulting from axisymmetric conditions. However, many of the processes in cells are non-axisymmetric in nature. To the best of our knowledge, there exist only a few studies that allow for general, non-axisymmetric shapes. Therefore, it is important to advance computational methods that can yield solutions for general conditions.

In the past, several computational models have been proposed for cell membranes. Depending on how the membrane is discretized, two categories can be distinguished: Models based on an explicit surface discretization, and models based on an implicit surface discretization. In the second category, the surface is captured by a phase field (Du and Wang, 2007) or level set function (Salac and Miksis, 2011) that is defined on the surrounding volume mesh. In the first category, the surface is captured directly by a surface mesh. The approach is particularly suitable if only surface effects are studied, such that no surrounding volume mesh is needed. This is the approach taken here. An example is to use Galerkin surface finite elements: The first corresponding 3D FE model for lipid bilayer membranes seems to be the formulation of Feng and Klug (2006) and Ma and Klug (2008). Their FE formulation is based on so-called subdivision surfaces (Cirak and Ortiz, 2001), which provide C^1 -continuous FE surface discretizations. Such discretizations are advantageous, since they do not require additional degrees of freedom as C^0 -continuous FE formulations do. Still, C^0 -continuous FEs have been considered to model red blood cell (RBC) membranes and their supporting protein skeleton (Dao et al., 2003; Peng et al., 2010), phase changes of lipid bilayers (Elliott and Stinner, 2010), and viscous cell membranes (Tasso and Buscaglia, 2013). Subdivision finite elements have been used to study confined cells (Kahraman et al., 2012). Lipid bilayers can also be modeled with so-called ‘solid shell’ (i.e. classical volume) elements instead of surface shell elements (Kloppel and Wall, 2011). Using solid elements, C^0 -continuity is sufficient, but the formulation is generally less efficient. For two-dimensional and axisymmetric problems also C^1 -continuous B-Spline and Hermite finite elements have been used to study membrane surface flows (Arroyo and DeSimone, 2009; Rahimi and Arroyo, 2012), cell invaginations (Rim et al., 2014), and cell tethering and adhesion (Rangarajan and Gao, 2015). The latter work also discusses the generalization to three-dimensional B-spline FE. For some problems it is also possible to use specific, Monge-patch FE discretizations (Rangamani et al., 2013, 2014).

There are also several works that do not use finite element approaches. Examples are numerical ODE integration (Agrawal and Steigmann, 2009), Monte Carlo methods (Ramakrishnan et al., 2010), molecular dynamics (Li and Lykotrafitis, 2012), finite difference methods (Lau et al., 2012; Gu et al., 2014) and mesh-free methods (Rosolen et al., 2013). There are also non-

Galerkin FE approaches that use triangulated surfaces, e.g. see [Jarić et al. \(1995\)](#); [Jie et al. \(1998\)](#).

For quasi-static simulations of liquid membranes and shells, the formulation needs to be stabilized. Therefore, various stabilization methods have been proposed considering artificial viscosity ([Ma and Klug, 2008](#); [Sauer, 2014](#)), artificial stiffness ([Kahraman et al., 2012](#)) and normal offsets – either as a projection of the solution (with intermediate mesh update steps) ([Sauer, 2014](#)), or as a restriction of the surface variation ([Rangarajan and Gao, 2015](#)). The instability problem is absent, if shear stiffness is present, e.g. due to an underlying cytoskeleton, like in RBCs ([Dao et al., 2003](#); [Peng et al., 2010](#); [Kloppel and Wall, 2011](#)). However, this setting does not apply to (purely) liquid membranes and shells.

Here, a novel FE formulation is presented for liquid shells that is based on an explicit, 3D surface discretization using NURBS ([Cottrell et al., 2009](#)). The following aspects are new:

- A theoretical study of the effective bulk and shear stiffness of the Helfrich bending model,
- the use of 3D, C^1 -continuous NURBS-based surface discretizations, considering purely displacement-based and
- mixed, LBB-conforming² finite elements,
- a comparison of both these FE formulations, illustrating the limitations of the former,
- the formulation, application and comparison of various stabilization schemes for quasi-static simulations
- that allow to accurately compute the in-plane stress state of the liquid, like the surface tension,
- the verification of the formulation by various analytical solutions,
- the possibility to capture complex, non-axisymmetric solutions, and
- new insight into the budding of cells and vesicles.

To the best of our knowledge, non-axisymmetric shapes have not been simulated to the same detail as is presented here.

The remainder of this paper is organized as follows: Sec. 2 presents an overview of the underlying theory of thin liquid shells. The governing weak form is presented and the model properties are discussed. Stabilization methods are then addressed in Sec. 3. The finite element formulation follows in Sec. 4. The formulation is verified and illustrated by several 3D numerical examples in Sec. 5. In particular, tethering and budding are studied. The paper then concludes with Sec. 6.

2 Summary of thin liquid shell theory

This section gives a brief overview of the governing equations of thin shell theory considering liquid material behavior. A much more detailed discussion can be found in [Sauer and Duong \(2015\)](#) and in the references therein.

²satisfying the Ladyzhenskaia-Babuška-Brezzi condition, see e.g. [Babuška \(1973\)](#); [Bathe \(1996\)](#)

2.1 Thin shell kinematics

The surface of the shell, denoted by \mathcal{S} , is described by the parameterization

$$\mathbf{x} = \mathbf{x}(\xi^\alpha), \quad \alpha = 1, 2, \quad (1)$$

where ξ^1 and ξ^2 are coordinates that can be associated with a flat 2D domain that is then mapped to \mathcal{S} by function (1). The surface is considered deformable. The deformation of \mathcal{S} is assessed in relation to a reference configuration \mathcal{S}_0 , described by the parameterization $\mathbf{X} = \mathbf{X}(\xi^\alpha)$. \mathcal{S} is considered here to coincide with \mathcal{S}_0 initially (e.g. at time $t = 0$), such that $\mathbf{x} = \mathbf{X}$ for $t = 0$. From these mappings, the tangent vectors $\mathbf{A}_\alpha = \mathbf{X}_{,\alpha}$ and $\mathbf{a}_\alpha = \mathbf{x}_{,\alpha}$ can be determined. Here $\dots_{,\alpha} := \partial \dots / \partial \xi^\alpha$ denotes the parametric derivative. From the tangent vectors, the surface normals

$$\mathbf{N} = \frac{\mathbf{A}_1 \times \mathbf{A}_2}{\|\mathbf{A}_1 \times \mathbf{A}_2\|}, \quad (2)$$

$$\mathbf{n} = \frac{\mathbf{a}_1 \times \mathbf{a}_2}{\|\mathbf{a}_1 \times \mathbf{a}_2\|}, \quad (3)$$

and the metric tensor components

$$A_{\alpha\beta} = \mathbf{A}_\alpha \cdot \mathbf{A}_\beta, \quad (4)$$

$$a_{\alpha\beta} = \mathbf{a}_\alpha \cdot \mathbf{a}_\beta \quad (5)$$

can be defined. From the inverses $[A^{\alpha\beta}] := [A_{\alpha\beta}]^{-1}$ and $[a^{\alpha\beta}] := [a_{\alpha\beta}]^{-1}$, the dual tangent vectors

$$\mathbf{A}^\alpha = A^{\alpha\beta} \mathbf{A}_\beta, \quad (6)$$

$$\mathbf{a}^\alpha = a^{\alpha\beta} \mathbf{a}_\beta \quad (7)$$

(with summation implied on repeated indices) can be introduced, such that $\mathbf{A}^\alpha \cdot \mathbf{A}_\beta = \delta_\beta^\alpha$ and $\mathbf{a}^\alpha \cdot \mathbf{a}_\beta = \delta_\beta^\alpha$, where δ_β^α is the Kronecker symbol. Further, we can define the surface identity tensors

$$\mathbf{I} = \mathbf{A}^\alpha \otimes \mathbf{A}_\alpha, \quad (8)$$

$$\mathbf{i} = \mathbf{a}^\alpha \otimes \mathbf{a}_\alpha, \quad (9)$$

such that the usual, 3D identity becomes

$$\mathbf{1} = \mathbf{I} + \mathbf{N} \otimes \mathbf{N} = \mathbf{i} + \mathbf{n} \otimes \mathbf{n}. \quad (10)$$

From the second derivatives of \mathbf{A}_α and \mathbf{a}_α one can define the curvature tensor components

$$B_{\alpha\beta} = \mathbf{A}_{\alpha,\beta} \cdot \mathbf{N}, \quad (11)$$

$$b_{\alpha\beta} = \mathbf{a}_{\alpha,\beta} \cdot \mathbf{n}, \quad (12)$$

allowing us to compute the mean, Gaussian and principal curvatures

$$H = \frac{1}{2} b^{\alpha\beta} a_{\alpha\beta}, \quad \kappa = \frac{\det[b_{\alpha\beta}]}{\det[a_{\alpha\beta}]}, \quad \kappa_{1/2} = H \pm \sqrt{H^2 - \kappa} \quad (13)$$

of surface \mathcal{S} , and likewise for \mathcal{S}_0 . Here, $b^{\alpha\beta} = a^{\alpha\gamma} b_{\gamma\delta} a^{\beta\delta}$.

For thin shells, the deformation between \mathcal{S}_0 and \mathcal{S} is fully characterized by $a_{\alpha\beta}$ and $b_{\alpha\beta}$, and their relation to $A_{\alpha\beta}$ and $B_{\alpha\beta}$. Two important quantities that characterize the in-plane part of the deformation are

$$I_1 = A^{\alpha\beta} a_{\alpha\beta} \quad (14)$$

and

$$I_2 = \det [A^{\alpha\beta}] \cdot \det [a_{\alpha\beta}] . \quad (15)$$

They define the invariants of the surface Cauchy Green tensors $\mathbf{C} = a_{\alpha\beta} \mathbf{A}^\alpha \otimes \mathbf{A}^\beta$ and $\mathbf{B} = A^{\alpha\beta} \mathbf{a}_\alpha \otimes \mathbf{a}_\beta$. The quantity $J = \sqrt{I_2}$ determines the change of surface area between \mathcal{S}_0 and \mathcal{S} . Given the parametric derivative of \mathbf{a}_α , the so-called co-variant derivative of \mathbf{a}_α is given by

$$\mathbf{a}_{\alpha;\beta} = (\mathbf{n} \otimes \mathbf{n}) \mathbf{a}_{\alpha,\beta} , \quad (16)$$

i.e. as the change of \mathbf{a}_α along \mathbf{n} . Introducing the Christoffel symbol $\Gamma_{\alpha\beta}^\gamma := \mathbf{a}^\gamma \cdot \mathbf{a}_{\alpha,\beta}$, we can also write

$$\mathbf{a}_{\alpha;\beta} = \mathbf{a}_{\alpha,\beta} - \Gamma_{\alpha\beta}^\gamma \mathbf{a}_{\gamma} . \quad (17)$$

For general vectors, $\mathbf{v} = v^\alpha \mathbf{a}_\alpha + v \mathbf{n}$, the parametric and co-variant derivative are considered to agree, i.e. $\mathbf{v}_{;\alpha} = \mathbf{v}_{,\alpha}$. Therefore, $v_{;\alpha} = v_{,\alpha}$, $\mathbf{n}_{;\alpha} = \mathbf{n}_{,\alpha}$, $(v^\alpha \mathbf{a}_\alpha)_{;\beta} = (v^\alpha \mathbf{a}_\alpha)_{,\beta}$ and

$$v_{;\beta}^\alpha = v_{,\beta}^\alpha + \Gamma_{\beta\gamma}^\alpha v^\gamma , \quad (18)$$

due to (10). Likewise definitions follow for the reference surface.

The variation and linearization of the above quantities can be found in [Sauer and Duong \(2015\)](#).

2.2 Quasi-static equilibrium

For negligible inertia, equilibrium of the thin shell is governed by the field equation ([Steigmann, 1999](#))

$$\mathbf{T}_{;\alpha}^\alpha + \mathbf{f} = \mathbf{0} , \quad (19)$$

where \mathbf{f} is a source term and

$$\mathbf{T}^\alpha = N^{\alpha\beta} \mathbf{a}_\beta + S^\alpha \mathbf{n} \quad (20)$$

is the traction vector acting on the surface normal to \mathbf{a}^α . It can be related to the stress tensor

$$\boldsymbol{\sigma} = N^{\alpha\beta} \mathbf{a}_\alpha \otimes \mathbf{a}_\beta + S^\alpha \mathbf{a}_\alpha \otimes \mathbf{n} \quad (21)$$

via Cauchy's formula $\mathbf{T}^\alpha = \boldsymbol{\sigma}^T \mathbf{a}^\alpha$, or equivalently $\mathbf{T} = \boldsymbol{\sigma}^T \boldsymbol{\nu}$ with $\boldsymbol{\nu} = \nu_\alpha \mathbf{a}^\alpha$ and $\mathbf{T} = \nu_\alpha \mathbf{T}^\alpha$. In Eqs. (20) and (21),

$$\begin{aligned} N^{\alpha\beta} &= \sigma^{\alpha\beta} + b_\gamma^\alpha M^{\gamma\beta} , \\ S^\alpha &= -M^{\beta\alpha}_{;\beta} \end{aligned} \quad (22)$$

are the in-plane and shear stress components acting on the cross section. The stress and bending moment components $\sigma^{\alpha\beta}$ and $M^{\alpha\beta}$ are given through constitution. Eqs. (19) and (22) are a consequence of momentum balance ([Sauer and Duong, 2015](#)). At the boundary of the surface, $\partial\mathcal{S}$, the boundary conditions

$$\begin{aligned} \mathbf{x} &= \bar{\boldsymbol{\varphi}} && \text{on } \partial_x \mathcal{S} , \\ \mathbf{t} &= \bar{\mathbf{t}} && \text{on } \partial_t \mathcal{S} , \\ m_\tau &= \bar{m}_\tau && \text{on } \partial_m \mathcal{S} \end{aligned} \quad (23)$$

can be prescribed. Here, m_τ is the bending moment component parallel to boundary $\partial\mathcal{S}$. For Kirchhoff-Love shells, bending moments perpendicular to boundary $\partial\mathcal{S}$, denoted m_ν , affect the boundary traction. Therefore the effective traction

$$\mathbf{t} := \mathbf{T} - (m_\nu \mathbf{n})' \quad (24)$$

is introduced ([Sauer and Duong, 2015](#)). We will consider $m_\nu = 0$ in the following.

2.3 Constitution

The focus here is on the quasi-static behavior of lipid bilayers, which can be described in the framework of hyperelasticity. For thin shells the stored energy function (per reference surface area) takes the form $W = W(a_{\alpha\beta}, b_{\alpha\beta})$, such that (Steigmann, 1999; Sauer and Duong, 2015)

$$\begin{aligned}\sigma^{\alpha\beta} &= \frac{2}{J} \frac{\partial W}{\partial a_{\alpha\beta}} , \\ M^{\alpha\beta} &= \frac{1}{J} \frac{\partial W}{\partial b_{\alpha\beta}} .\end{aligned}\tag{25}$$

From this we can then evaluate the in-plane stress $N^{\alpha\beta}$ and the shear S^α according to (22). For convenience, we further define $\tau^{\alpha\beta} := J\sigma^{\alpha\beta}$, $M_0^{\alpha\beta} := JM^{\alpha\beta}$ and $N_0^{\alpha\beta} := JN^{\alpha\beta}$. The bending behavior of lipid bilayers is commonly described by the bending model of Helfrich (1973)

$$w = k(H - H_0)^2 + k^*\kappa ,\tag{26}$$

which is an energy density per current surface area. Here k is the bending modulus, k^* is the Gaussian modulus and H_0 denotes the so-called spontaneous curvature caused by the presence of certain proteins. Based on (26), we consider the following two constitutive models:

2.3.1 Area-compressible lipid bilayer

Combining the Helfrich energy with an energy resulting from the surface area change, we write

$$W = Jw + \frac{K}{2}(J - 1)^2 .\tag{27}$$

Here a simple quadratic term for the compressible part is considered, since the area change of lipid bilayers is very small before rupture occurs (typically $|J - 1| < 4\%$). According to (25) and (22), the stress and moment components then become

$$\begin{aligned}\sigma^{\alpha\beta} &= (K(J - 1) + k\Delta H^2 - k^*\kappa) a^{\alpha\beta} - 2k\Delta H b^{\alpha\beta} , \\ M^{\alpha\beta} &= (k\Delta H + 2k^*H) a^{\alpha\beta} - k^*b^{\alpha\beta} , \\ N^{\alpha\beta} &= (K(J - 1) + k\Delta H^2) a^{\alpha\beta} - k\Delta H b^{\alpha\beta} ,\end{aligned}\tag{28}$$

where $\Delta H := H - H_0$.

Remark: Here, k and k^* are material constants that have the units *strain energy per current surface area*. In principle, also Jk and Jk^* could be regarded as material constants that now have the units *strain energy per reference surface area*. This alternative would lead to different expressions for $\sigma^{\alpha\beta}$ and $N^{\alpha\beta}$.

2.3.2 Area-incompressible lipid bilayer

Since K is usually very large for lipid-bilayers, one may as well consider the surface to be fully area-incompressible. Using the Lagrange multiplier approach, we now have

$$W = Jw + qg ,\tag{29}$$

where the incompressibility constraint

$$g := J - 1 = 0\tag{30}$$

is enforced by the Lagrange multiplier q , which is an independent variable that needs to be accounted for. Physically, it corresponds to a surface tension. The stress and moment components now become

$$\begin{aligned}\sigma^{\alpha\beta} &= (q + k \Delta H^2 - k^* \kappa) a^{\alpha\beta} - 2k \Delta H b^{\alpha\beta} , \\ M^{\alpha\beta} &= (k \Delta H + 2k^* H) a^{\alpha\beta} - k^* b^{\alpha\beta} , \\ N^{\alpha\beta} &= (q + k \Delta H^2) a^{\alpha\beta} - k \Delta H b^{\alpha\beta} ,\end{aligned}\tag{31}$$

which is identical to (28) for $q = Kg$.

As K becomes larger and larger both models approach the same solution. So from a physical point of view it may not make a big difference which model is used. Computationally, model (27) is easier to handle but can become inaccurate for large K as is shown in Sec. 5. In analytical approaches, often (29) is preferred as it usually simplifies the solution. Examples for the latter case are found in Baesu et al. (2004) and Agrawal and Steigmann (2009); the former case is considered in the original work of Helfrich (1973).

2.3.3 Model properties

In both models, the membrane part only provides bulk stiffness, but lacks shear stiffness. For quasi-static computations the model can thus become unstable and should be stabilized, as is discussed in Sec. 3. Interestingly, the bending part of the Helfrich model can contribute an in-plane shear stiffness, which is shown in the following.

We first introduce the surface tension γ of the surface as the average trace of the stress tensor, giving

$$\gamma := \frac{1}{2} \boldsymbol{\sigma} : \mathbf{i} = \frac{1}{2} N_\alpha^\alpha .\tag{32}$$

For both (28) and (31) we find

$$\gamma = q - k H_0 \Delta H ,\tag{33}$$

where $q = Kg$ in the former case. It can be seen that for $H_0 \neq 0$, the bending part contributes to the surface tension. The surface tension is therefore not given by the membrane part alone (Rangamani et al., 2014). For the compressible case, the effective bulk modulus can then be determined from

$$K_{\text{eff}} := \frac{\partial \gamma}{\partial J} ,\tag{34}$$

i.e. as the change of γ w.r.t J . We find

$$K_{\text{eff}} = K + k H_0 H/J ,\tag{35}$$

since $\partial H/\partial J = -H/J$. Likewise we can define the effective shear modulus from

$$\mu_{\text{eff}} := J a_{\alpha\gamma} \frac{\partial N_{\text{dev}}^{\alpha\beta}}{2 \partial a_{\gamma\delta}} a_{\beta\delta} ,\tag{36}$$

i.e. as the change of the deviatoric stress w.r.t to the deviatoric deformation (characterized by $a_{\gamma\delta}/J$). The deviatoric in-plane stress is given by

$$N_{\text{dev}}^{\alpha\beta} := N^{\alpha\beta} - \gamma a^{\alpha\beta} .\tag{37}$$

We find

$$N_{\text{dev}}^{\alpha\beta} = k \Delta H (H a^{\alpha\beta} - b^{\alpha\beta})\tag{38}$$

for both (28) and (31). Evaluating (36) thus gives

$$\mu_{\text{eff}} = Jk (3H^2 - 2HH_0 - \kappa)/2 . \quad (39)$$

The model therefore provides stabilizing shear stiffness if $3H^2 > 2HH_0 + \kappa$. Since this is not always the case (e.g. for flat surface regions), additional shear stabilization should be provided in general. This is discussed in Sec. 3. The value of μ_{eff} is discussed in detail in the examples of Sec. 5. It is shown that μ_{eff} can sufficiently stabilize the problem such that no additional shear stabilization is needed. It is also shown that μ_{eff} does not necessarily need to be positive to avoid instabilities. Geometric stiffening, arising in large deformations, can also stabilize the shell.

2.4 Weak form

The computational solution technique proposed here is based on the weak form governing the mechanics of the lipid bilayer. Consider a kinematically admissible variation of the surface denoted by $\delta\mathbf{x} \in \mathcal{V}$. Such a variation of \mathcal{S} causes variations of \mathbf{a}_α , \mathbf{n} , $a_{\alpha\beta}$ and $b_{\alpha\beta}$. Contracting field equation (19) with $\delta\mathbf{x}$, integrating over \mathcal{S} and applying Stokes' theorem leads to the weak form (Sauer and Duong, 2015)

$$G = G_{\text{int}} - G_{\text{ext}} = 0 \quad \forall \delta\mathbf{x} \in \mathcal{V} , \quad (40)$$

with

$$\begin{aligned} G_{\text{int}} &= \int_{\mathcal{S}} \frac{1}{2} \delta a_{\alpha\beta} \sigma^{\alpha\beta} da + \int_{\mathcal{S}} \delta b_{\alpha\beta} M^{\alpha\beta} da , \\ G_{\text{ext}} &= \int_{\mathcal{S}} \delta\mathbf{x} \cdot \mathbf{f} da + \int_{\partial_t \mathcal{S}} \delta\mathbf{x} \cdot \mathbf{t} ds + \int_{\partial_m \mathcal{S}} \delta\mathbf{n} \cdot m_\tau \boldsymbol{\nu} ds . \end{aligned} \quad (41)$$

Denoting the in-plane and out-of-plane components of $\delta\mathbf{x}$ by w_α and w , such that $\delta\mathbf{x} := w_\alpha \mathbf{a}^\alpha + w \mathbf{n}$, we find that

$$\delta a_{\alpha\beta} = w_{\alpha;\beta} + w_{\beta;\alpha} - 2w b_{\alpha\beta} . \quad (42)$$

Thus, the first part of G_{int} can be split into in-plane and out-of-plane contributions as

$$\int_{\mathcal{S}} \frac{1}{2} \delta a_{\alpha\beta} \sigma^{\alpha\beta} da = G_\sigma^{\text{in}} + G_\sigma^{\text{out}} , \quad (43)$$

with

$$G_\sigma^{\text{in}} = \int_{\mathcal{S}} w_{\alpha;\beta} \sigma^{\alpha\beta} da \quad (44)$$

and

$$G_\sigma^{\text{out}} = - \int_{\mathcal{S}} w b_{\alpha\beta} \sigma^{\alpha\beta} da . \quad (45)$$

In principle – although not needed here – the second part of G_{int} can also be split into in-plane and out-of-plane contributions (Sauer and Duong, 2015). In the area-incompressible case, we additionally have to satisfy the weak form of constraint (30),

$$G_g = \int_{\mathcal{S}_0} \delta q g dA = 0 \quad \forall \delta q \in \mathcal{Q} , \quad (46)$$

where \mathcal{Q} is an admissible space for the variation of Lagrange multiplier q .

3 Liquid shell stabilization

As noted above, the system is unstable for quasi-static computations. There are two principal ways to stabilize the system without modifying/affecting the original problem. They are discussed in the following two sections and then summarized in Sec. 3.3.

3.1 Adding stiffness

Firstly, the system can be stabilized by adding a stabilization stress $\sigma_{\text{sta}}^{\alpha\beta}$ to $\sigma^{\alpha\beta}$ in order to provide additional stiffness. This stress can be defined from a (convex) shear energy or from numerical viscosity. An elegant and accurate way to stabilize the system is to add the stabilization stress only to the in-plane contribution (44) while leaving the out-of-plane contribution (45) unchanged. The advantage of this approach is that the out-of-plane part, responsible for the shape of the bilayer, is not affected by the stabilization, at least not in the continuum limit of the surface discretization. There are several different ways to define the stabilization stress, which we will group into two categories. An overview of all the options is then summarized in Tab. 1.

3.1.1 In-plane shear and bulk stabilization

The first category goes back to Sauer (2014), who used it to stabilize liquid membranes governed by constant surface tension. The stabilization stress for such membranes requires shear and bulk contributions. Those are given for example by the stabilization stress

$$\sigma_{\text{sta}}^{\alpha\beta} = \mu/J(A^{\alpha\beta} - a^{\alpha\beta}) , \quad (47)$$

based on numerical stiffness, and

$$\sigma_{\text{sta}}^{\alpha\beta} = \mu/J(a_{\text{pre}}^{\alpha\beta} - a^{\alpha\beta}) , \quad (48)$$

based on numerical viscosity. Here $a_{\text{pre}}^{\alpha\beta}$ denotes the value of $a^{\alpha\beta}$ at the preceding computational step. These stabilization stresses are then only included within Eq. (44) and not in Eq. (45), and the resulting two stabilization schemes are denoted ‘A’ (for (47)) and ‘a’ (for (48)) following Sauer (2014). This reference shows that scheme ‘a’ is highly accurate and performs much better than scheme ‘A’. It is also shown that applying the stabilization stresses (47) and (48) only to the in-plane part is much more accurate than applying it throughout the system (i.e. in both Eqs. (44) and (45)), which we denote as schemes ‘A-t’ and ‘a-t’.

3.1.2 Sole in-plane shear stabilization

If the surface tension is not constant, as in the lipid bilayer models introduced above, only shear stabilization is required. Therefore, the following new category of stabilization schemes is defined. Consider a split of the surface Cauchy-Green tensor into dilatational and deviatoric parts, such that $\mathbf{C} = J\widehat{\mathbf{C}}$, where $\widehat{\mathbf{C}} := J^{-1}\mathbf{C}$ describes only the deviatoric deformation (since $\det \widehat{\mathbf{C}} = 1$). The stored energy function of an elastic membrane can then be defined for example by

$$W = \frac{K}{4}(J^2 - 1 - 2 \ln J) + \frac{\mu}{2}(\widehat{I}_1 - 2) , \quad (49)$$

where $\widehat{I}_1 = I_1/J$ is the first invariant of $\widehat{\mathbf{C}}$. The first term in (49) captures purely dilatoric deformations, while the second part captures purely deviatoric deformations. The formulation is analogous to the 3D case described for example in [Wriggers \(2008\)](#). Since the bilayer energy introduced in [Sec. 2.3](#) already contains a bulk part, we now only need to consider the contribution

$$W_{\text{sta}} = \frac{\mu}{2}(\widehat{I}_1 - 2) \quad (50)$$

to derive the new stabilization scheme. From (25) we then find the stabilization stress

$$\sigma_{\text{sta}}^{\alpha\beta} = \frac{\mu}{J^2} \left(A^{\alpha\beta} - \frac{I_1}{2} a^{\alpha\beta} \right), \quad (51)$$

or

$$\tau_{\text{sta}}^{\alpha\beta} = \frac{\mu}{J} \left(A^{\alpha\beta} - \frac{I_1}{2} a^{\alpha\beta} \right). \quad (52)$$

As before, this stress will only be applied to [Eq. \(44\)](#) and not in [Eq. \(45\)](#), even though it has been derived from a potential and should theoretically apply to both terms. Following earlier nomenclature we denote this scheme by ‘A-s’. Replacing $A^{\alpha\beta}$ by $a_{\text{pre}}^{\alpha\beta}$ in (52) gives

$$\tau_{\text{sta}}^{\alpha\beta} = \frac{\mu}{J^*} \left(a_{\text{pre}}^{\alpha\beta} - \frac{I_1^*}{2} a^{\alpha\beta} \right), \quad (53)$$

with $J^* := \sqrt{\det a_{\alpha\beta} / \det a_{\alpha\beta}^{\text{pre}}}$ and $I_1^* := a_{\text{pre}}^{\alpha\beta} a_{\alpha\beta}$, which is an alternative shear-stabilization scheme based on numerical viscosity. We denote it ‘a-s’. If stresses (52) and (53) are applied throughout the system (i.e. to both (44) and (45)), we denote the corresponding schemes ‘A-st’ and ‘a-st’.

If the shell is (nearly) area-incompressible the two stabilization methods of [Sec. 3.1.1](#) and [3.1.2](#) can behave identical, as can be seen by [example 5.1](#).

3.1.3 Relation to physical viscosity

Schemes (48) and (53) are related to physical viscosity. Considering (near) area-incompressibility ($J^* = J = 1$), the viscous stress for a Newtonian fluid is given by

$$\sigma_{\text{visc}}^{\alpha\beta} = -\nu \dot{a}^{\alpha\beta} \quad (54)$$

([Aris, 1989](#); [Rangamani et al., 2013, 2014](#)), where $\dot{a}^{\alpha\beta} = -a^{\alpha\gamma} \dot{a}_{\gamma\delta} a^{\delta\beta}$. Considering the first order rate approximation

$$\dot{a}^{\alpha\beta} \approx \frac{1}{\Delta t} \left(a^{\alpha\beta} - a_{\text{pre}}^{\alpha\beta} \right), \quad (55)$$

and a small time step ($I_1^* \approx 2$), immediately leads to expressions (48) and (53) with

$$\nu = \mu \Delta t. \quad (56)$$

3.2 Normal projection

The second principal way to stabilize the system consists of a simple projection of the formulation onto the solution space defined by the normal surface direction. We apply this step directly to the discretized formulation as was proposed by [Sauer \(2014\)](#). According to this, for the given

discrete system of linear equations for displacement increment $\Delta \mathbf{u}$ given by $\mathbf{K} \Delta \mathbf{u} = -\mathbf{f}$, the reduced system for increment $\Delta \mathbf{u}_{\text{red}} = \mathbf{P} \Delta \mathbf{u}$ is simply obtained as

$$\mathbf{K}_{\text{red}} \Delta \mathbf{u}_{\text{red}} = -\mathbf{f}_{\text{red}}, \mathbf{K}_{\text{red}} := \mathbf{P} \mathbf{K} \mathbf{P}^T, \mathbf{f}_{\text{red}} := \mathbf{P} \mathbf{f}, \quad (57)$$

where

$$\mathbf{P} := \begin{bmatrix} \mathbf{n}_1^T & \mathbf{0}^T & \dots & \mathbf{0}^T \\ \mathbf{0}^T & \mathbf{n}_2^T & \dots & \mathbf{0}^T \\ \vdots & \vdots & \ddots & \vdots \\ \mathbf{0}^T & \mathbf{0}^T & \dots & \mathbf{n}_{n_{\text{no}}}^T \end{bmatrix} \quad (58)$$

is a projection matrix defined by the nodal normal vectors \mathbf{n}_I . Since this method can lead to distorted FE meshes, a mesh update can be performed by applying any of the stabilization techniques discussed above. If this is followed by a projection step at the same load level, a dependency on parameter μ is avoided.

For NURBS discretizations, the computation of the normal \mathbf{n}_I corresponding to control point I is not trivial, since the control points generally do not lie on the surface. The control points can be projected onto the actual surface in order to evaluate the normal at the projection point. As a simplification of this approach one can also work with the approximate normal obtained at the current location of the initial projection point. The difference between the two approaches is very small as Fig. 1 shows. There are minor differences in the locations of the projection points

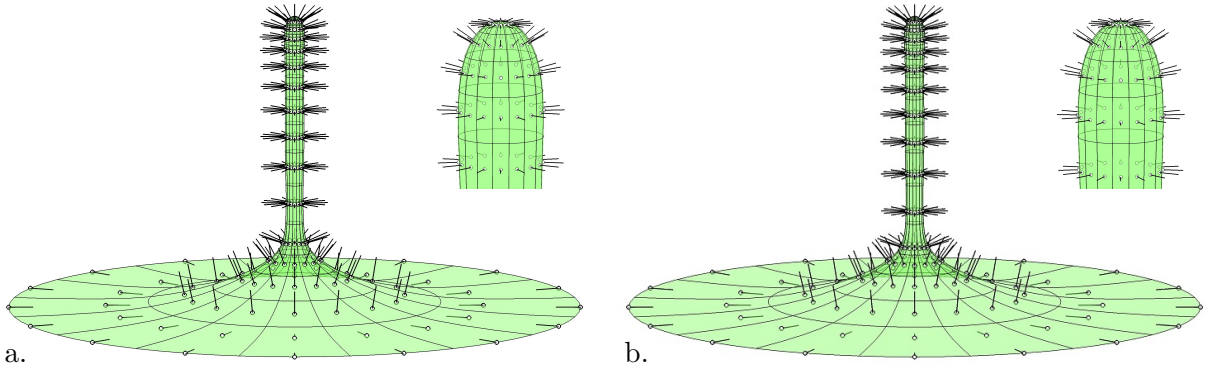


Figure 1: Search direction \mathbf{n}_I for stabilization scheme ‘P’: a. Considering the normals at the projected control points; b. Considering the normals at the current location of the initially projected control points.

where \mathbf{n}_I is evaluated. But \mathbf{n}_I itself does not change much. In the example considered here and in Sauer (2014), no significant difference was therefore found in the numerical results. In order to solve the reduced problem (57) appropriate boundary conditions are needed. Boundary conditions can be applied before reduction or they can be suitably adapted to the reduced system. This is also shown in Fig. 1. In this example (see Sec. 5.3) the vertical displacement at the outer two and inner two rings of nodes is prescribed. After a mesh update at a given solution step no further vertical displacement can therefore occur on those nodes. But the nodes can still move radially. Therefore one can simply replace \mathbf{n}_I at those nodes by radial unit vectors.

Remark: For liquid droplets, stabilization scheme ‘P’ shows superior accuracy over all other schemes (Sauer, 2014). However this is not the case for area-incompressible surfaces: For a curved surface, non-zero values of $\Delta \mathbf{u}_{\text{red}}$ lead to a change in surface area. In regions of non-zero

curvature, $\Delta \mathbf{u}_{\text{red}}$ will therefore tend to be zero, yielding scheme ‘P’ ineffective. This is confirmed by the results in Sec. 5.3.

3.3 Summary of the stabilization schemes

The nine stabilization schemes presented above are summarized in Tab. 1. They can be grouped

class	scheme	stab. stress $\sigma_{\text{sta}}^{\alpha\beta}/\mu$	application of $\sigma_{\text{sta}}^{\alpha\beta}$	dependence
A	A	$(A^{\alpha\beta} - a^{\alpha\beta})/J$	only in (44)	only on μ
	A-t	$(A^{\alpha\beta} - a^{\alpha\beta})/J$	both in (44) & (45)	only on μ
	A-s	$(A^{\alpha\beta} - \frac{1}{2}I_1 a^{\alpha\beta})/J^2$	only in (44)	only on μ
	A-st	$(A^{\alpha\beta} - \frac{1}{2}I_1 a^{\alpha\beta})/J^2$	both in (44) & (45)	only on μ
a	a	$(a_{\text{pre}}^{\alpha\beta} - a^{\alpha\beta})/J$	only in (44)	on μ and n_t
	a-t	$(a_{\text{pre}}^{\alpha\beta} - a^{\alpha\beta})/J$	both in (44) & (45)	on μ and n_t
	a-s	$(a_{\text{pre}}^{\alpha\beta} - \frac{1}{2}I_1^* a^{\alpha\beta})/J^{*2}$	only in (44)	on μ and n_t
	a-st	$(a_{\text{pre}}^{\alpha\beta} - \frac{1}{2}I_1^* a^{\alpha\beta})/J^{*2}$	both in (44) & (45)	on μ and n_t
P	P	0	–	on nodal \mathbf{n}_I

Table 1: Summary of the stabilization schemes presented in Sec. 3.1.1 and 3.1.2

into three classes: **A**, **a** and **P**. The schemes of class **A** depend only on μ but require this value to be quite low. The schemes of class **a** also depend on the number of computational steps, n_t . If this number is high the schemes provide stiffness without adding much stress. The shell is then stabilized without modifying the solution much, even when μ is high. Scheme ‘P’ depends on the nodal projection vector \mathbf{n}_I , which is usually taken as the surface normal. The performance of the different stabilization schemes is investigated in the examples of Sec. 5.

4 FE formulation

This section presents a general finite element formulation for lipid bilayers using both material models of Sec. 2.3. The formulation applies to general 3D surfaces. It is based on the solid shell formulation of Duong et al. (2015).

4.1 FE approximation

The geometry of the reference surface and the current surface are approximated by the finite element interpolations

$$\mathbf{X} \approx \mathbf{N} \mathbf{X}_e \quad (59)$$

and

$$\mathbf{x} \approx \mathbf{N} \mathbf{x}_e, \quad (60)$$

where $\mathbf{N} := [N_1 \mathbf{1}, \dots, N_{n_e} \mathbf{1}]$ is a $(3 \times 3n_e)$ array containing the n_e nodal shape functions $N_I = N_I(\xi^1, \xi^2)$ of element Ω^e defined in parameter space. $\mathbf{X}_e := [\mathbf{X}_1^T, \dots, \mathbf{X}_{n_e}^T]^T$ and

$\mathbf{x}_e := [\mathbf{x}_1^T, \dots, \mathbf{x}_{n_e}^T]^T$ contain the n_e nodal position vectors of Ω^e . In order to ensure C^1 -continuity of the surface, NURBS-based shape functions are used (Borden et al., 2011). The tangent vectors of the surface are thus approximated by

$$\mathbf{A}_\alpha = \frac{\partial \mathbf{X}}{\partial \xi^\alpha} \approx \mathbf{N}_{,\alpha} \mathbf{X}_e \quad (61)$$

and

$$\mathbf{a}_\alpha = \frac{\partial \mathbf{x}}{\partial \xi^\alpha} \approx \mathbf{N}_{,\alpha} \mathbf{x}_e, \quad (62)$$

From these, the normal vectors of the surface are then determined from (2) and (3). The variation of \mathbf{x} and \mathbf{a}_α are approximated in the same manner, i.e.

$$\delta \mathbf{x} \approx \mathbf{N} \delta \mathbf{X}_e \quad (63)$$

and

$$\delta \mathbf{a}_\alpha \approx \mathbf{N}_{,\alpha} \delta \mathbf{x}_e. \quad (64)$$

Based on these expressions, all the kinematical quantities discussed in Sec. 2.1 as well as their variation (Sauer and Duong, 2015) can be evaluated.

4.2 Discretized weak form

Inserting the above interpolations into the weak form of Sec. 2.4 leads to the approximated weak form

$$G \approx \sum_{e=1}^{n_{el}} G^e = \sum_{e=1}^{n_{el}} (G_{\text{int}}^e - G_{\text{ext}}^e). \quad (65)$$

The internal virtual work of each finite element is given by (Duong et al., 2015)

$$G_{\text{int}}^e = \delta \mathbf{x}_e^T (\mathbf{f}_{\text{int}\sigma}^e + \mathbf{f}_{\text{int}M}^e), \quad (66)$$

with the FE force vectors due to the membrane stress $\sigma^{\alpha\beta}$ and the bending moment $M^{\alpha\beta}$

$$\mathbf{f}_{\text{int}\sigma}^e := \int_{\Omega^e} \sigma^{\alpha\beta} \mathbf{N}_{,\alpha}^T \mathbf{a}_\beta \, da, \quad (67)$$

and

$$\mathbf{f}_{\text{int}M}^e := \int_{\Omega^e} M^{\alpha\beta} (\mathbf{N}_{,\alpha\beta}^T - \Gamma_{\alpha\beta}^\gamma \mathbf{N}_{,\gamma}^T) \mathbf{n} \, da. \quad (68)$$

Following decomposition (43), $\mathbf{f}_{\text{int}\sigma}^e$ can be split into the in-plane and out-of-plane contributions (Sauer et al., 2014)

$$\begin{aligned} \mathbf{f}_{\text{inti}}^e &:= \mathbf{f}_{\text{int}\sigma}^e - \mathbf{f}_{\text{into}}^e, \\ \mathbf{f}_{\text{into}}^e &:= - \int_{\Omega^e} \sigma^{\alpha\beta} b_{\alpha\beta} \mathbf{N}^T \mathbf{n} \, da. \end{aligned} \quad (69)$$

The external virtual work for each FE due to the external loads \mathbf{f} , \mathbf{t} and m_τ is given by (Duong et al., 2015)

$$G_{\text{ext}}^e = \delta \mathbf{x}_e^T (\mathbf{f}_{\text{ext}f}^e + \mathbf{f}_{\text{ext}t}^e + \mathbf{f}_{\text{ext}m}^e), \quad (70)$$

with

$$\begin{aligned} \mathbf{f}_{\text{ext}f}^e &:= \int_{\Omega^e} \mathbf{N}^T \mathbf{f} \, da, \\ \mathbf{f}_{\text{ext}t}^e &:= \int_{\partial_t \Omega^e} \mathbf{N}^T \mathbf{t} \, ds, \\ \mathbf{f}_{\text{ext}m}^e &:= \int_{\partial_m \Omega^e} \mathbf{N}_{,\alpha}^T \nu^\alpha m_\tau \mathbf{n} \, ds. \end{aligned} \quad (71)$$

For the complete linearization of these terms, see [Sauer et al. \(2014\)](#), [Duong et al. \(2015\)](#) and [Appendix A](#). The linearization requires the material tangents of $\sigma^{\alpha\beta}$ and $M^{\alpha\beta}$. For the material models in (28) and (31) these are given in [Sauer and Duong \(2015\)](#). For the stabilization schemes in [Sec. 3.1.1](#) the tangent is given in [Sauer \(2014\)](#), while the tangent for schemes ‘A-s’ and ‘A-st’ (see (52)) in [Sec. 3.1.2](#) is

$$c^{\alpha\beta\gamma\delta} := 2 \frac{\partial \tau^{\alpha\beta}}{\partial a_{\gamma\delta}} = \frac{\mu}{J} \left(\frac{I_1}{2} a^{\alpha\beta} a^{\gamma\delta} - I_1 a^{\alpha\beta\gamma\delta} - a^{\alpha\beta} A^{\gamma\delta} - A^{\alpha\beta} a^{\gamma\delta} \right). \quad (72)$$

For schemes ‘a-s’ and ‘a-st’, the terms I_1 and J are simply substituted by I_1^* and J^* , respectively. Here, $a^{\alpha\beta\gamma\delta}$ is given in [Sauer and Duong \(2015\)](#).

4.3 Area constraint

For the area-incompressible case, a further step is to discretize the constraint and the corresponding Lagrange multiplier. For the latter, we write

$$q \approx \mathbf{L} \mathbf{q}_e, \quad (73)$$

as in [Eq. \(60\)](#). Here $\mathbf{L} := [L_1, \dots, L_{m_e}]$ is a $(1 \times m_e)$ array containing the m_e nodal shape functions $L_I = L_I(\xi^1, \xi^2)$ of surface element Ω^e , and $\mathbf{q}_e := [q_1, \dots, q_{m_e}]^T$ contains the m_e nodal Lagrange multipliers of the element. It follows that

$$\delta q \approx \mathbf{L} \delta \mathbf{q}_e, \quad (74)$$

such that weak constraint (46) becomes

$$G_g \approx \sum_{e=1}^{n_{el}} G_g^e, \quad (75)$$

where

$$G_g^e = \delta \mathbf{q}_e^T \mathbf{g}^e, \quad (76)$$

with

$$\mathbf{g}^e := \int_{\Omega_0^e} \mathbf{L}^T g \, dA. \quad (77)$$

The linearization of \mathbf{g}^e , needed for the following solution procedure, is provided in [Appendix B](#).

4.4 Solution procedure

The elemental vectors $\mathbf{f}_{\text{int}\sigma}^e$, $\mathbf{f}_{\text{int}M}^e$, $\mathbf{f}_{\text{ext}f}^e$, $\mathbf{f}_{\text{ext}t}^e$, $\mathbf{f}_{\text{ext}m}^e$ and \mathbf{g}^e are assembled into the global vectors \mathbf{f} and \mathbf{g} by adding corresponding entries. The discretized weak form then reads

$$\delta \mathbf{x}^T \mathbf{f}(\mathbf{x}, \mathbf{q}) + \delta \mathbf{q}^T \mathbf{g}(\mathbf{x}) = 0, \quad \forall \delta \mathbf{x} \in \mathcal{V}^h \ \& \ \delta \mathbf{q} \in \mathcal{Q}^h, \quad (78)$$

where \mathbf{x} , \mathbf{q} , $\delta \mathbf{x}$ and $\delta \mathbf{q}$ are global vectors containing all nodal deformations, Lagrange multipliers and their variations. \mathcal{V}^h and \mathcal{Q}^h are corresponding discrete spaces. [Eq. \(78\)](#) is satisfied if $\mathbf{f} = \mathbf{0}$ and $\mathbf{g} = \mathbf{0}$ at nodes where no Dirichlet BC apply. These two nonlinear equations are then solved with Newton’s method for the unknowns \mathbf{x} and \mathbf{q} . We note that the discretization of \mathbf{x} and q should satisfy the LBB-condition ([Babuška, 1973](#); [Bathe, 1996](#)). For that, we consider here C^1 -continuous, bi-quadratic NURBS interpolation for \mathbf{x} and C^0 -continuous, bi-linear Lagrange interpolation for q . If no constraint is present (like in model (27)), the parts containing \mathbf{q} and \mathbf{g} are simply skipped. A comparison between the different models ((27) and (29)) is presented in [Sec. 5](#).

4.5 Rotational constraints

To constrain rotations, we add the constraint potential

$$\Pi_n = \int_{\mathcal{L}_0} \frac{\epsilon}{2} (\mathbf{n} - \bar{\mathbf{n}}) \cdot (\mathbf{n} - \bar{\mathbf{n}}) dS \quad (79)$$

to the shell formulation. This approach can be used to apply rotations at boundaries, to fix rotations at symmetry boundaries, and to equalize normals at patch boundaries. The particular boundary under consideration is denoted as \mathcal{L}_0 in the reference configuration. ϵ is a penalty parameter. The variation, linearization and FE discretization of (79) is discussed in [Duong et al. \(2015\)](#).

4.6 Normalization

For a numerical implementation, the above expressions need to be normalized. We normalize the geometry and deformation by some length scale L , i.e. $\bar{\mathbf{X}} = \mathbf{X}/L$ and $\bar{\mathbf{x}} = \mathbf{x}/L$, where the bar indicates non-dimensional quantities, and non-dimensionalize all the kinematics based on this. The material parameters are chosen to be normalized by parameter k , which has the unit [force \times length]. The non-dimensional material parameters thus are

$$\begin{aligned} \bar{k} &= 1, \\ \bar{k}^* &= k^*/k, \\ \bar{K} &= K L^2/k, \\ \bar{\mu} &= \mu L^2/k, \\ \bar{\epsilon} &= \epsilon L/k. \end{aligned} \quad (80)$$

With the chosen normalization parameters k and L , the normalization of stress and moment components become³

$$\begin{aligned} \bar{q} &= q L^2/k, \\ \bar{\sigma}^{\alpha\beta} &= \sigma^{\alpha\beta} L^2/k, \\ \bar{M}^{\alpha\beta} &= M^{\alpha\beta} L/k, \end{aligned} \quad (81)$$

while the normalization of the loading follows as

$$\begin{aligned} \bar{\mathbf{f}} &= \mathbf{f} L^3/k, \\ \bar{\mathbf{t}} &= \mathbf{t} L^2/k, \\ \bar{m}_\tau &= m_\tau L/k. \end{aligned} \quad (82)$$

5 Numerical examples

To illustrate the performance of the proposed finite element model, four examples – marked by increasing computational complexity – are presented here. The first three examples have analytical solutions that are used for model verification.

5.1 Pure bending and stretching of a flat strip

The first example considers the bending of a flat strip, with dimension $S \times L$, by applying the rotation $\Theta/2$ at the ends of the strip as is shown in Fig. 2a. Further, a uniform stretch, with

³supposing that the parameters ξ^α carry units of length, so that $a_{\alpha\beta}$ and $a^{\alpha\beta}$ become dimensionless

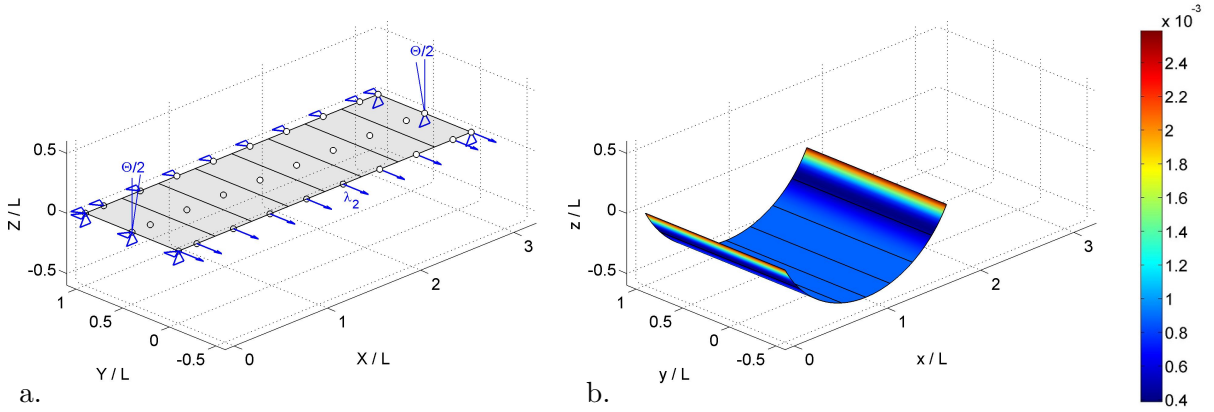


Figure 2: Pure bending: a. initial FE configuration and boundary conditions (for $S = \pi L$ discretized with $m = 8$ elements); b. current FE configuration for an imposed rotation and stretch of $\Theta/2 = \pi/3$ and $\lambda_2 = 1.5$. The color shows the relative error in the mean curvature, defined as $e_H := 1 - H_{\text{FE}}/H_{\text{exact}}$, considering model (29) without any stabilization.

magnitude λ_2 , is applied as shown in the figure. The remaining boundaries are supported as shown. In particular, the rotation along the boundaries at $Y = 0$ and $Y = L$ is not constrained. We will study the problem by examining the support reactions $M = M(\Theta, \lambda_2)$ (the distributed moment along $X = 0$) and $N = N(\Theta, \lambda_2)$ (the traction along $Y = 0$). The analytical solution for this problem is given by [Sauer and Duong \(2015\)](#). According to this, the strip deforms into a curved sheet with dimension $s \times \ell = \lambda_1 S \times \lambda_2 L$ and constant mean curvature

$$H = \frac{\kappa_1}{2}, \quad (83)$$

where $\lambda_1 = s/S$, $\lambda_2 = \ell/L$ and $\kappa_1 = \Theta/s$ are the in-plane stretches and the out-of-plane curvature of the strip. Further,

$$[a^{\alpha\beta}] = \begin{bmatrix} \lambda_1^{-2} & 0 \\ 0 & \lambda_2^{-2} \end{bmatrix} \quad (84)$$

and

$$[b^{\alpha\beta}] = \begin{bmatrix} \kappa_1 \lambda_1^{-2} & 0 \\ 0 & 0 \end{bmatrix}. \quad (85)$$

With this, the in-plane stress components become

$$\begin{aligned} N_1^1 &= q - k H^2, \\ N_2^2 &= q + k H^2 \end{aligned} \quad (86)$$

both for the area-incompressible model of (29) and the compressible model of (27) with $q = K(J - 1)$. For the considered boundary conditions, $N_1^1 = 0$, so that

$$q = k H^2, \quad (87)$$

and we thus have the support reaction (per current length) $N := N_2^2 = 2k H^2$ along $Y = 0$ and $Y = \ell$. Per reference length this becomes $N_0 = \lambda_1 N$. The bending moment necessary to support the applied rotation (along $X = 0$ and $X = \pi R$) becomes ([Sauer and Duong, 2015](#))

$$M = k H \quad (88)$$

per current length of the support (or $M_0 = \lambda_2 M$ per reference length). If the special case $k^* = -k/2$ (Canham, 1970) is considered, there is no bending in the Y -direction.

For the area-incompressible model of (29), we have $\lambda_1 = 1/\lambda_2$. For the area-compressible case according to model (27), we can determine λ_1 from (87) with $J = \lambda_1 \lambda_2$, giving

$$\lambda_1 = \frac{1}{\lambda_2} \left[\frac{k}{K} H^2 + 1 \right]. \quad (89)$$

The two cases are solved numerically using the computational setup shown in Fig. 2. The FE mesh is discretized by m elements along X . The parameter t is introduced to apply the rotation $\Theta = t\pi/6$ and stretch $\lambda_2 = 1 + t/2$ by increasing t linearly from 0 to 1 in n_t steps, where n_t is chosen as a multiple of m . The mean curvature then follows as $H = \Theta/(2\lambda_1 S)$. For the unconstrained case, λ_1 is then the solution of the cubic equation

$$\lambda_1^3 \lambda_2 - \lambda_1^2 - \frac{\Theta^2}{4\bar{K}} = 0, \quad (90)$$

with $\bar{K} = KS^2/k$. Numerically, the rotation is applied according to (79) considering the penalty parameter $\epsilon = 100 n_x k/L$. Fig. 3 shows the FE solution and analytical solution for $M_0(t)$ and $N_0(t)$, normalizing M by k/L and N by k/L^2 .

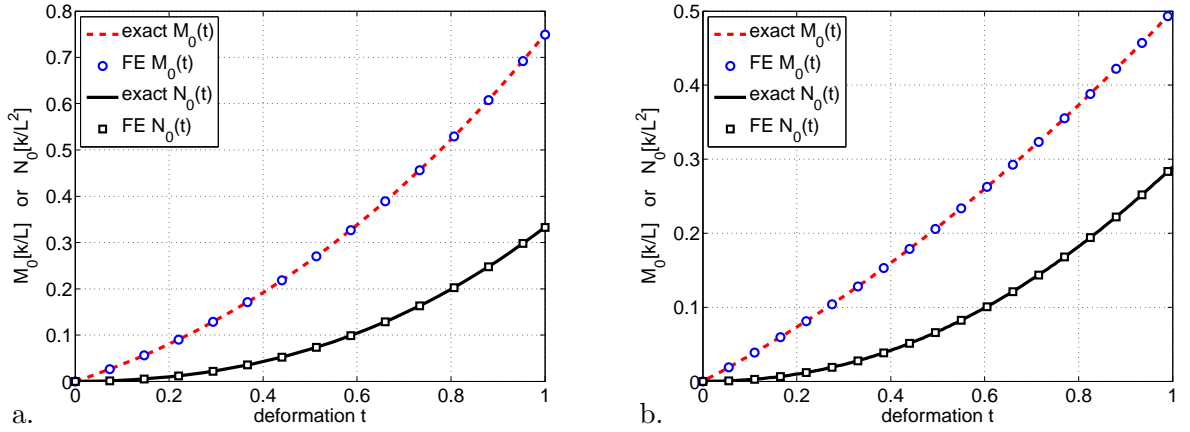


Figure 3: Pure bending: distributed boundary moment $M_0(t)$ and normal traction $N_0(t)$ as obtained analytically and computationally for a. the area-incompressible model (29) and b. the area-compressible model (27) for $\bar{K} = 2.5$.

Next, the accuracy of the different stability schemes is studied in detail by examining the L_2 -error of the solution, defined by

$$L_2 := \sqrt{\frac{1}{SL} \int_{S_0} \|\mathbf{u}_{\text{exact}} - \mathbf{u}_{\text{FE}}\|^2 dA}, \quad (91)$$

and the error in M and N , defined by

$$E_{MN} := \frac{|M_{\text{exact}} - M_{\text{FE}}|}{M_{\text{exact}}} + \frac{|N_{\text{exact}} - N_{\text{FE}}|}{N_{\text{exact}}}, \quad (92)$$

where M_{FE} and N_{FE} are the computed mean values along the respective boundaries. The first error is a measure of the kinematic accuracy, while the second is a measure of the kinetic

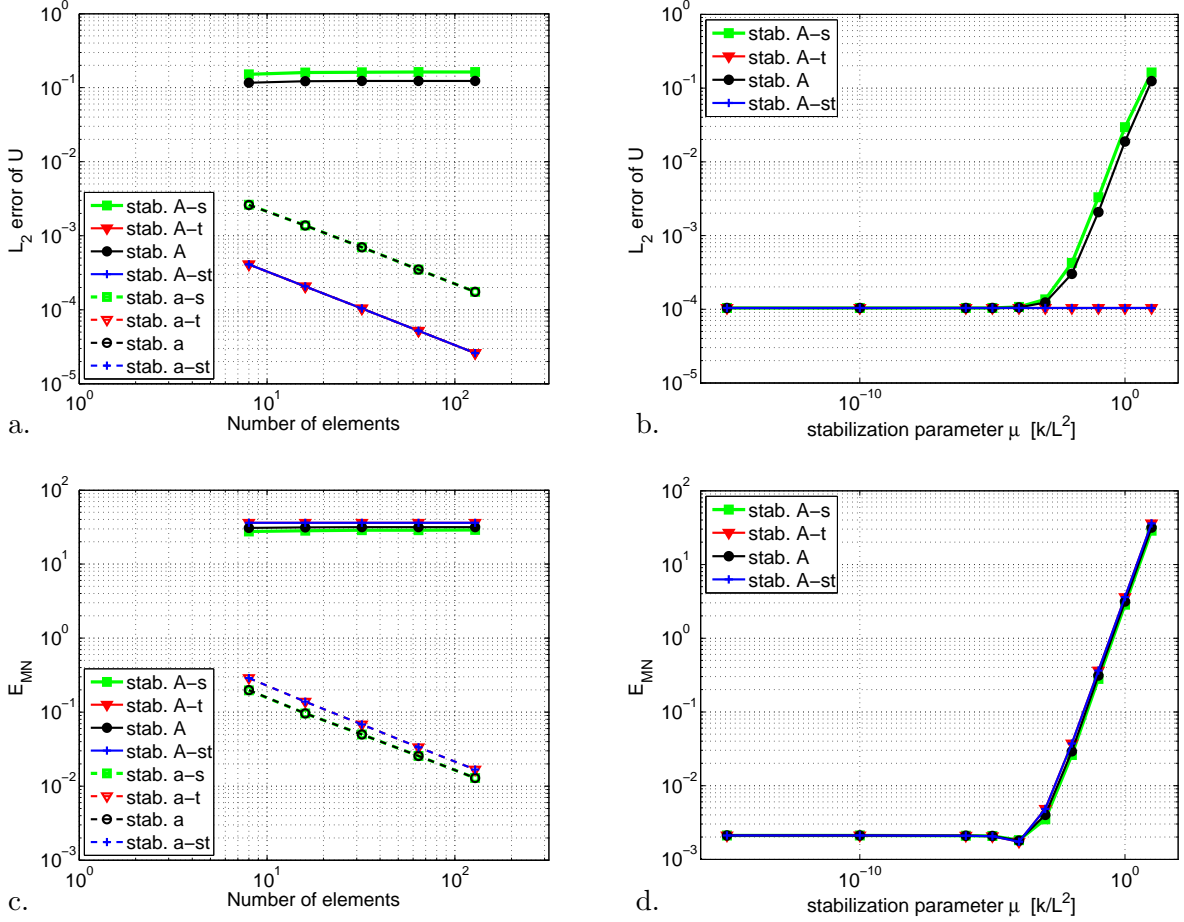


Figure 4: Pure bending: accuracy for the area-incompressible model (29): a. L_2 -error vs. m considering stabilization classes **A** and **a** with $\bar{\mu} = 10$ and $n_t = 12.5m$; b. L_2 -error vs. μ considering stabilization class **A** with $m = 32$; c.-d. same as a.-b., but now for error E_{MN} . Considered is $\Theta/2 = \pi/3$ and $\lambda_2 = 1.5$.

accuracy. Fig. 4 shows the two errors for the area-incompressible model of Eq. (29). Looking at the L_2 -error, schemes ‘A-t’, ‘A-st’, ‘a-t’ and ‘a-st’ perform best. In case of error E_{MN} , schemes ‘a’ and ‘a-s’ perform best. Class **A** generally converges with μ , but it may not converge with the number of elements for high values of μ . Interestingly, the L_2 -error of scheme ‘A-t’ and ‘A-st’ is not affected by μ , as schemes ‘A’ and ‘A-s’ are. For sufficiently low μ (for $m = 32$ about $\bar{\mu} < 10^{-3}$), the accuracy of class **A** (both in L_2 and E_{MN}) reaches that of class **a** and then only improves with mesh refinement. Class **A** with low μ may even surpass class **a** with high μ . But generally, class **a** is more accurate and robust (as μ does not need to be very small). There is no clear favourite in class **a** for this test case.

Fig. 5 shows the two errors for the area-compressible model of Eq. (27) considering $\bar{K} = 2.5$. In case of the L_2 -error, scheme ‘a’ performs best, while for error E_{MN} , scheme ‘a-s’ is best. As before, class **A** is poor for large μ , but reaches (and may surpass) the accuracy of class **a** at some μ depending on m .

As the plots show, not a single stabilization scheme stands out here and the accuracy depends both on the model and the error measure. In general, all schemes are suitable to solve the problem. If class **A** is used, the value of μ needs to be suitably low. For class **a** even large values for μ can be used. In this example it is even possible to set $\mu = 0$ in the code. This works

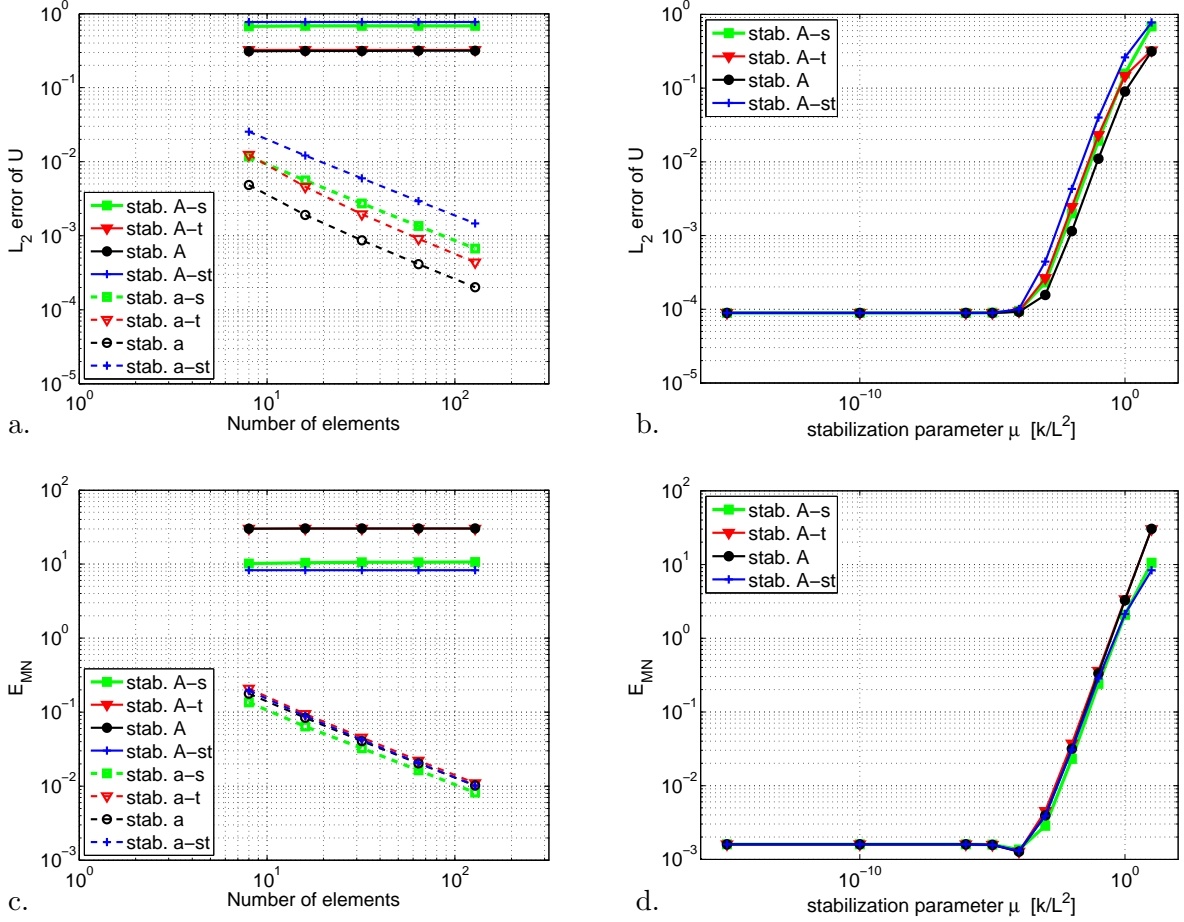


Figure 5: Pure bending: accuracy of the area-compressible model (27): a. L_2 -error vs. m considering stabilization classes **A** and **a** with $\bar{\mu} = 10$ and $n_t = 12.5m$; b. L_2 -error vs. μ considering stabilization class **A** with $m = 32$; c.–d. same as a.–b., but now for error E_{MN} . Considered is $\bar{K} = 2.5$, $\Theta/2 = \pi/3$ and $\lambda_2 = 1.5$.

since the effective shear stiffness according to (39) is positive here, i.e. $\mu_{\text{eff}} = 3JkH^2/2 > 0$. For other problems μ_{eff} can be negative, and stabilization is required.

5.2 Inflation of a sphere

The second example considers the inflation of a spherical cell. Contrary to the previous example, the FE mesh now also contains interfaces between NURBS patches. Since the surface area increases during inflation, potential (27) is considered. For this model, the in-plane traction component, given in (28), is

$$N^{\alpha\beta} = N_a a^{\alpha\beta} + N_b b^{\alpha\beta}, \quad (93)$$

with

$$\begin{aligned} N_a &:= k \Delta H^2 + K (J - 1), \\ N_b &:= -k \Delta H. \end{aligned} \quad (94)$$

The initial radius of the sphere is denoted by R , the initial volume is denoted by $V_0 = 4\pi R^3/3$. The cell remains spherical during inflation, so that we can obtain an analytical reference solution.

The current radius during inflation shall be denoted by r , the current volume by $V = 4\pi r^3/3$. Considering the surface parameterization

$$\mathbf{x}(\phi, \theta) = \begin{bmatrix} r \cos \phi \sin \theta \\ r \sin \phi \sin \theta \\ -r \cos \theta \end{bmatrix}, \quad (95)$$

we find

$$[a^{\alpha\beta}] = \frac{1}{r^2} \begin{bmatrix} 1/\sin^2 \theta & 0 \\ 0 & 1 \end{bmatrix}, \quad (96)$$

$b^{\alpha\beta} = -a^{\alpha\beta}/r$ and $H = -1/r$ for this example. The traction vector $\mathbf{T} = \nu_\alpha \mathbf{T}^\alpha$ on a cut $\perp \boldsymbol{\nu}$ thus becomes

$$\mathbf{T} = (N_a - N_b/r) \boldsymbol{\nu} + S^\alpha \nu_\alpha \mathbf{n} \quad (97)$$

according to (20). The in-plane component $T_\nu := N_a - N_b/r$ must equilibrate the current pressure according to the well-known relation

$$p = \frac{2T_\nu}{r}. \quad (98)$$

We can thus establish the analytical pressure-volume relation

$$\bar{p}(\bar{V}) = 2\bar{H}_0 \bar{V}^{-\frac{2}{3}} - 2\bar{H}_0^2 \bar{V}^{-\frac{1}{3}} + 2\bar{K} \left(\bar{V}^{\frac{1}{3}} - \bar{V}^{-\frac{1}{3}} \right), \quad (99)$$

normalized according to the definitions $\bar{p} := pR^3/k$, $\bar{V} := V/V_0$, $\bar{H}_0 := H_0R$ and $\bar{K} := KR^2/k$.

Fig. 6 shows the computational setup of the problem. The computational domain consists of

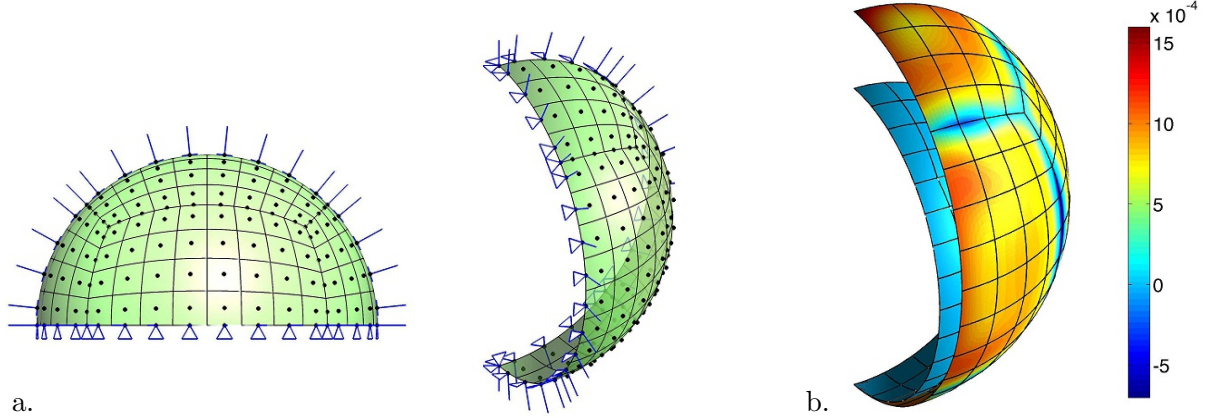


Figure 6: Sphere inflation: a. initial FE configuration and boundary conditions (for mesh $m = 8$); b. current FE configuration for an imposed volume of $\bar{V} = 2$ compared to the initial configuration; the colors show the relative error in the surface tension T_ν .

a quarter sphere discretized with four NURBS patches. The quarter sphere contains $3m^2/2$ elements where m is the number of elements along the equator of the quarter sphere. At the boundaries and at the patch interfaces C^1 -continuity is enforced using (79) with $\epsilon = 4000mk/R$. The area bulk modulus is taken as $K = 5k/R^2$, while k^* is taken as zero. Two cases are considered: $H_0 = 0$ and $H_0 = 1/R$. Fig. 7 shows that the computational $p(V)$ -data converge to the exact analytical result of (99). Here the pressure error

$$e_p = \frac{|p_{\text{exact}} - p_{\text{FE}}|}{p_{\text{exact}}} \quad (100)$$

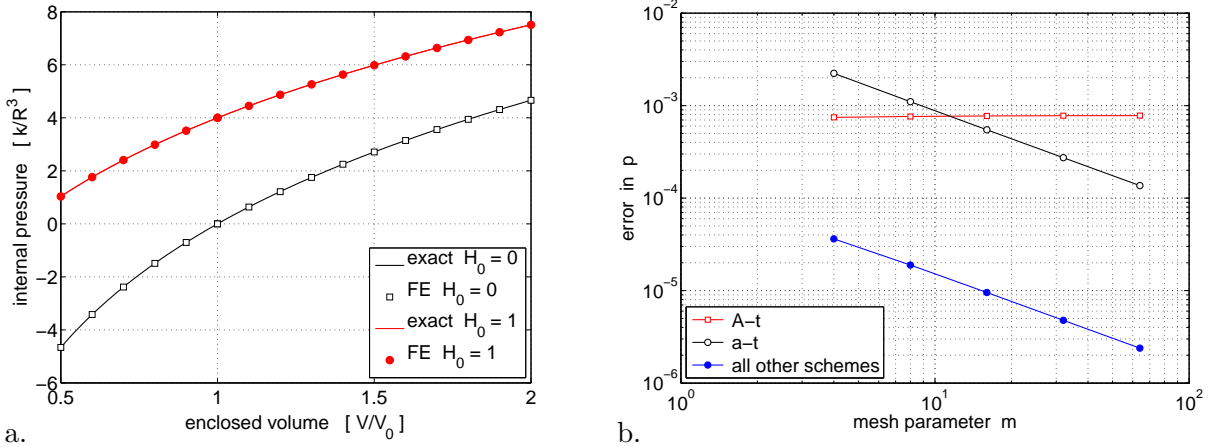


Figure 7: Sphere inflation: a. pressure-volume relation; b. FE convergence for the different stabilization schemes.

is examined for $H_0 = 1/R$ and $\bar{V} = 2$ considering the 9 stabilization schemes of Tab. 1 with $\bar{\mu} = 0.01$ for class **A** and $\bar{\mu} = 1$ and $n_t = 5m$ for class **a**. For schemes ‘A’, ‘A-s’, ‘A-st’, ‘a’, ‘a-s’, ‘a-st’ and ‘P’ this error converges nicely (and is indistinguishable in the figure). Only schemes ‘A-t’ and ‘a-t’ behave significantly different. They introduce further errors that only converge if μ is decreased or n_t is increased. The reason why all other schemes have equal error, is that here the error is actually determined by the penalty parameter ϵ used within patch constraint (79). The error stemming from the stabilization methods (apart from ‘A-t’ and ‘a-t’) is insignificant compared to that. It is interesting to note that ‘A-st’ and ‘a-st’ perform much better than ‘A-t’ and ‘a-t’, even though no shear is present in the analytical solution. ‘A-st’ and ‘a-st’ can therefore be considered as the best choices here, since they are the most efficient schemes to implement.

We finally note that for a sphere $\mu_{\text{eff}} = JkH(H - H_0)$, where $H = -1/r$. Thus $\mu_{\text{eff}} > 0$ for $H < H_0$, which is the case here.

5.3 Drawing of a tube

Tube-like shapes are one of the most common non-trivial shapes in biological cell membranes. They can be observed in the endoplasmic reticulum (Shibata et al., 2006, 2009; Hu et al., 2009) and mitochondria (Fawcett, 1981; Griparic and van der Blik, 2001; Shibata et al., 2009), where individual tubules or a complex network of tubules co-exist. The tubes can also be formed when a membrane is pulled by actin or microtubule polymerization, or by molecular motors attached to membranes but walking on cytoskeletal filaments (Terasaki et al., 1986; Waterman-Storer and Salmon, 1998; Koster et al., 2003; Itoh et al., 2005). These situations can be modeled by means of a lateral force that acts on a membrane. An analytical solution for this problem has been obtained by Derényi et al. (2002) by assuming axisymmetry and infinitely long tubes, which we use to verify our finite element formulation. The dynamics of tether formation and relaxation have been also studied by Rahimi and Arroyo (2012).

To simulate the tube drawing process we consider the setup shown in Fig. 8. The cell membrane is modeled as a circular, initially flat disc with initial radius L . The effect of the surrounding membrane is captured by the boundary tension σ (w.r.t. the current boundary length). The surface is described by material model (27). L and k are used for normalization. The remaining

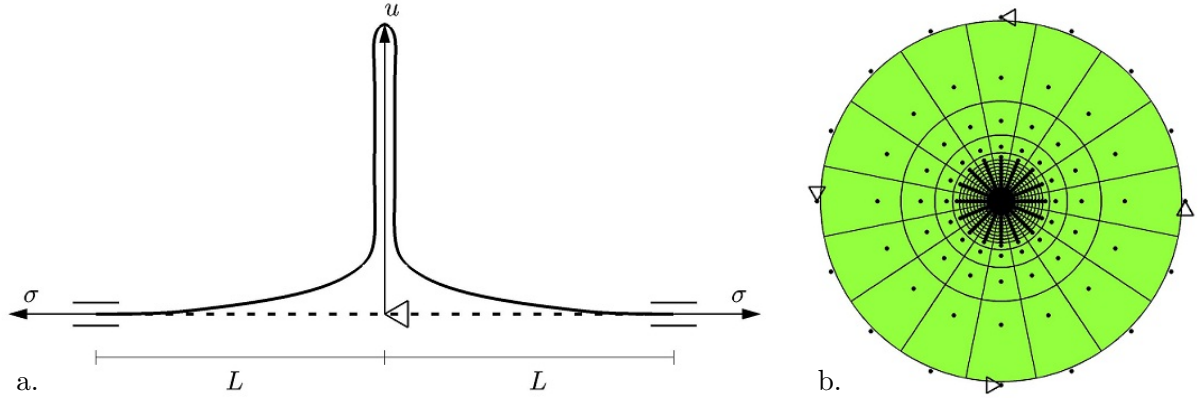


Figure 8: Tube drawing: a. boundary conditions and b. coarse FE mesh of the initial configuration. The dots show the control points of the NURBS discretization.

material parameters are chosen as $\bar{k} = -0.7k$ and $K = 20,000k/L^2$. H_0 is taken as zero. We consider $\sigma \in \{100, 200, 400, 800\}k/L^2$. Stabilization scheme ‘A-s’ is considered with $\mu = 0.1k/L^2$. The shell is clamped at the boundary, but free to move in the in-plane direction. The traction $\mathbf{t} = \sigma\boldsymbol{\nu}$ is imposed and applied numerically via (71.2). Even though \mathbf{t} is constant during deformation, the boundary length ds appearing in $\mathbf{f}_{\text{ext}}^e$ changes and has to be linearized. This is, for example, discussed in Sauer (2014). At the center, the displacement u is imposed on the initially flat, circular surface. To prevent rigid rotations, selected nodes are supported as shown in Fig. 8b.

Fig. 8b also shows one of the chosen finite element discretizations of the initial configuration. Quadratic, NURBS-based, C^1 -continuous finite elements are used. For those, the outer ring of control points lies outside of the mesh; their distance to the center is therefore slightly larger than L . A finer discretization is chosen at the center, where the tube is going to form. The chosen NURBS discretization degenerates at the center, such that the C^1 -continuity is lost there. It is regained if displacement u is applied not only to the central control point but also to the first ring of control points around the center. This ensures that the tangent plane remains horizontal at the tip. Likewise, a horizontal tangent is enforced at the outer boundary by fixing the height of the outer two rings of control points.

Fig. 9 shows the deformed surface at $u = L$, considering different values of the far-field surface tension σ . The surface tension affects the slenderness of the appearing tube. Derényi et al. (2002) showed from theoretical considerations⁴ that the tube radius is

$$a = \frac{1}{2}\sqrt{\frac{k}{\sigma}}, \quad (101)$$

while the steady force during tube drawing is

$$P_0 = 2\pi\sqrt{\sigma k}. \quad (102)$$

These values are confirmed by our computations, which is illustrated in Fig. 10.

⁴Assuming that the tube is sufficiently long and can be idealized by a perfect cylinder.

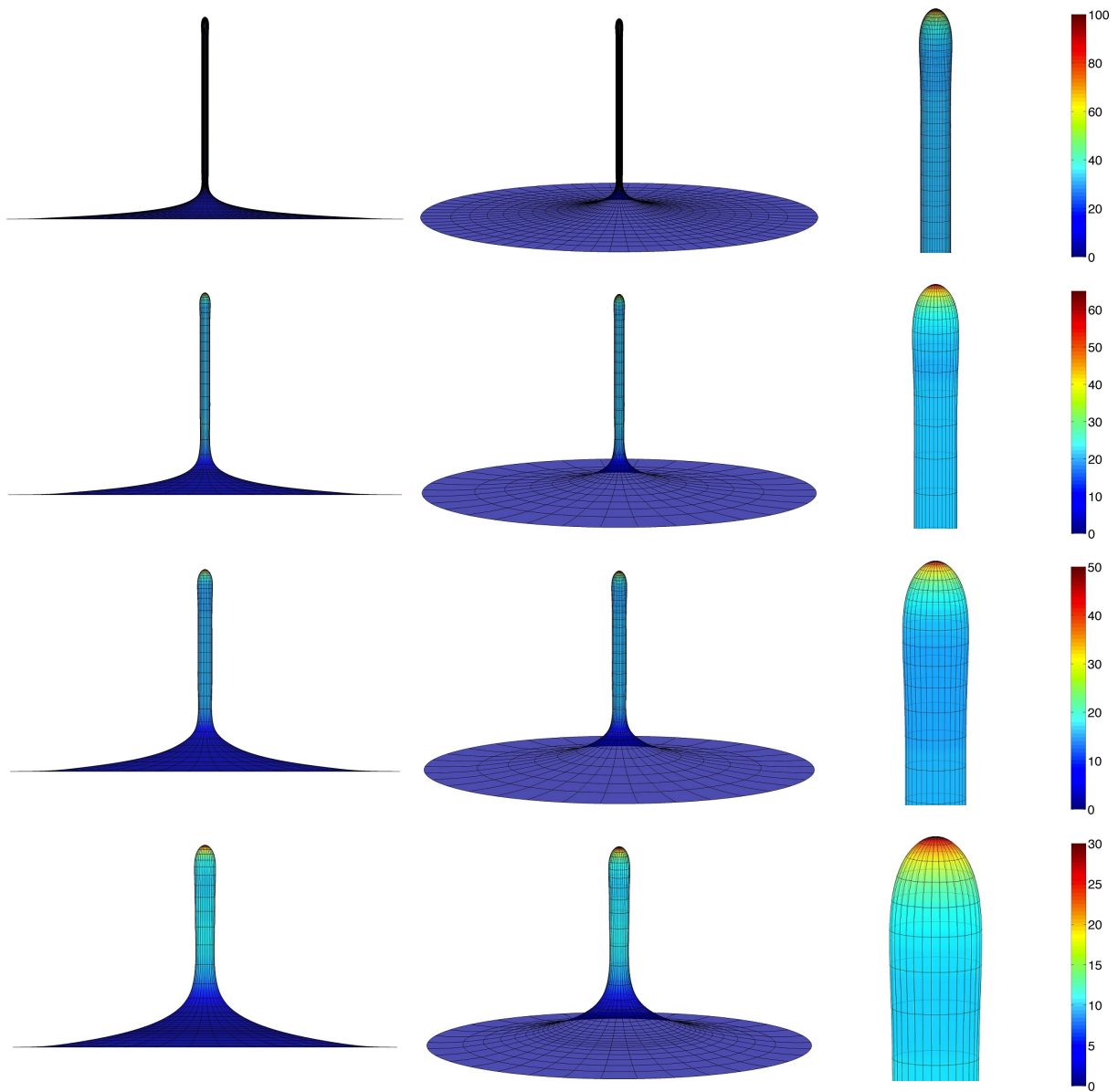


Figure 9: Tube drawing: Results for $\sigma \in \{100, 200, 400, 800\} k/L^2$ (bottom to top); colorscale shows the mean curvature H normalized by L^{-1} .

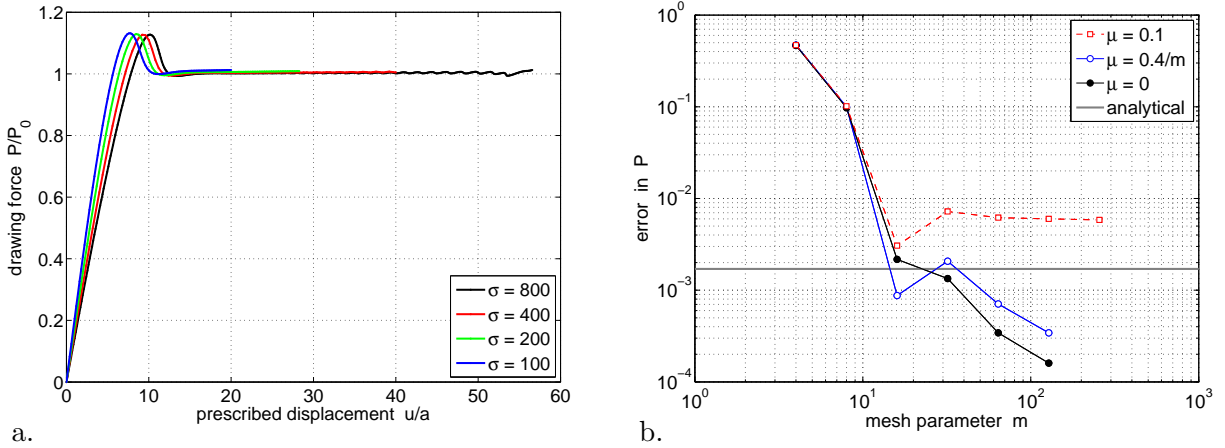


Figure 10: Tube drawing: a. load-displacement curve; b. FE convergence.

The left inset shows the force-displacement relation during drawing. Oscillations appear in the numerical solution due to the mesh discretization error. They are more pronounced for more slender tubes, as the black curve in Fig. 10a shows. They disappear upon mesh refinement, as the solution converges. The convergence of P_0 for $\sigma = 200k/L^2$ and $u = L$ ($= 28.28a$) is shown in Fig. 10b by examining the error

$$e(P_0^{\text{FE}}) := \frac{|P_0^{\text{ref}} - P_0^{\text{FE}}|}{P_0^{\text{ref}}}, \quad (103)$$

where P_0^{ref} is the FE solution for $m = 256$ and $\mu = 0$. The mesh sequence given in Tab. 2 is used for the convergence study. For the convergence study, the following stabilization cases are

m	$n_{\text{el}} = 4m^2$	$n_{\text{no}} = 4m(m+1)$	$\bar{\mu}$
4	64	80	1/10
8	256	288	1/20
16	1024	1088	1/40
32	4096	4224	1/80
64	16384	16640	1/160
128	65336	66048	1/320
256	262144	263168	1/640

Table 2: tube drawing: computational parameters (number of surface elements n_{el} , number of control points n_{no} and stability parameter $\bar{\mu}$) for the convergence study of Fig. 10b.

considered:

1. scheme ‘A-s’ with fixed $\bar{\mu} = 0.1$,
2. scheme ‘A-s’ with varying $\bar{\mu}$, as specified in Tab. 2,
3. scheme ‘P’ using the solution of case 1 as initial guess,
4. scheme ‘P’ using the solution of case 2 as initial guess,
5. no stabilization ($\mu = 0$), using the solution of case 2 as initial guess.

It turns out that scheme ‘P’ does not at all improve the results obtained by scheme ‘A-s’, probably due to the issue noted in the remark of Sec. 3.2. Case 1 does not converge below an

error of about 0.6%, which reflects the error caused by $\bar{\mu} = 0.1$. Case 5 works due to the inherent shear stiffness of the Helfrich model given in (39). For the cylindrical part, $\bar{\mu}_{\text{eff}} = 3H^2/2 > 0$. With $H = -1/(2a)$ follows $\bar{\mu}_{\text{eff}} = 3/(2a^2)$. At the tip, the principal curvatures are equal ($\kappa_1 = \kappa_2$), so that $\bar{\mu}_{\text{eff}} = \kappa_1^2 > 0$. At the tip the curvature is almost twice as large as the cylinder curvature (i.e. $\kappa_1 \approx -2/a$), so that $\bar{\mu}_{\text{eff}} \approx 4k/a^2$. In the cap, $\bar{\mu}_{\text{eff}}$ ranges in between these two extreme values, and so μ_{eff} is always positive. The initial flat disk has $\mu_{\text{eff}} = 0$, so that stabilization is needed for the initial step. In all cases, the error reported in Fig. 10b is assessed by comparison to the finest mesh of case 2. From this we can find that the analytical solution itself has an error of about 0.2%, due to its underlying assumptions.

5.4 Cell budding

The last example considers the budding of spherical cells. The example is used to demonstrate the capabilities of the proposed computational model, in particular in the context of non-trivial and non-axisymmetric deformations.

5.4.1 Motivation

It is known that protein adsorption can mediate shape changes in biological membranes (Zimmerberg and Kozlov, 2006; McMahon and Gallop, 2005; Kozlov et al., 2014; Shi and Baumgart, 2015). The lipid membrane deforms whenever its curvature is incompatible with the inherent structure of a protein, giving rise to a spontaneous curvature. Such protein-induced spontaneous curvature is common in many important biological phenomena such as endocytosis (Buser and Drubin, 2013; Kukulski et al., 2012; Peter et al., 2004), cell motility (Keren, 2011) and vesicle formation (Gruenberg and Stenmark, 2004). For example, in endocytosis, a clathrin protein coat is formed on the membrane which is incompatible with the membrane curvature, thus driving the out-of-plane shape changes, finally leading to fission. Moreover, another set of curvature generating proteins, the so-called BAR proteins (Peter et al., 2004; Kukulski et al., 2012), play an important role in modulating shape changes leading to fission in the later stages of endocytosis.

In this example, we use the proposed finite element formulation to study the shape changes in membranes due to protein-induced spontaneous curvature. This spontaneous curvature usually depends on the concentration of proteins adsorbed onto the membrane. In obtaining the shapes, we assume that any proteins that are bound to the membrane do not diffuse and are concentrated in a specific region (Walther et al., 2006; Agrawal and Steigmann, 2009; Karotki et al., 2011; Kishimoto et al., 2011; Rangamani et al., 2014). Such processes are common in all endocytosis related phenomena, where it is known that the clathrin protein coat does not diffuse in the membrane once adsorbed. Therefore, our example aims at helping to understand the shapes arising in the early stages of endocytosis.

5.4.2 Computational setup

For our example, we consider a hemi-spherical cell with initial radius R ; the cell surface is clamped at the boundary, but free to expand radially as is shown in Fig. 11. On the tip of the cell, within the circular region of radius $0.2R$, a constant spontaneous curvature \bar{H}_0 is prescribed. Unless otherwise specified, model (27) is used with the material parameters $\bar{k}^* = -0.7$ and $\bar{K} = 10,000$, while k and R are used for normalization according to Sec. 4.6 and remain unspecified. Further, stabilization scheme ‘A-s’ is used with $\bar{\mu} = 0.01$. The FE

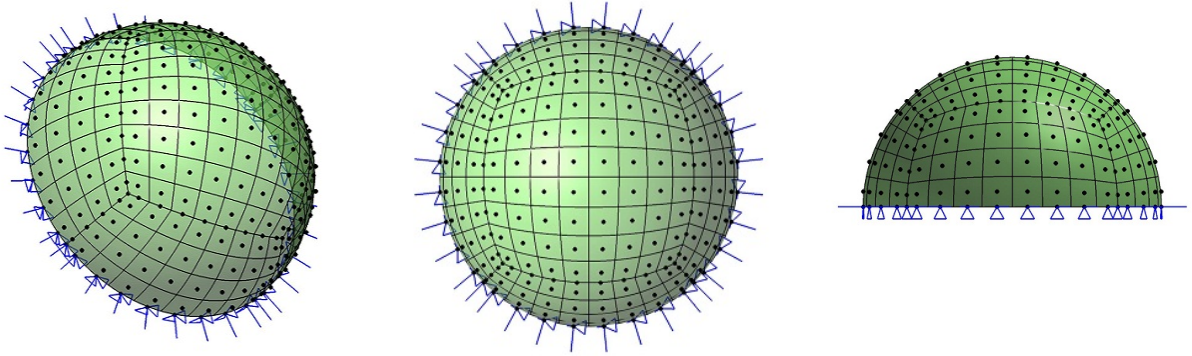


Figure 11: Cell budding: initial configuration, FE discretization and boundary conditions. The boundary normal is fixed and the boundary nodes are only free to move in the radial direction.

discretization shown in Fig. 11, consisting of five NURBS patches, is used. Where the patches meet, constraint (79) is added to ensure rotational continuity and moment transfer. Constraint (79) is also used to fix the boundary normal. The actual FE mesh is much finer than in Fig. 11 and uses 12228 elements (64 times more than in the figure). The penalty parameter of the rotational constraint is $\bar{\epsilon} = 6,400$. Gaussian quadrature is considered, using 3×3 points for surface integrals and 4 points for line integrals.

5.4.3 Bud shapes

In past numerical studies, axisymmetric bud shapes have been reported, e.g. Walani et al. (2015). These shapes should be a natural solution due to the axisymmetry of the problem. However, as is shown below, non-axisymmetric solutions are also possible, and in fact energetically favorable, indicating that axisymmetric solutions can become unfavored. This is illustrated by considering

case	bud shape	H_0 region	stabilization	$\bar{\mu}$	in-plane stress state
1	axisymmetric	circle	A-s	0.01	hydro-static
2	general	circle	A-s	0.01	hydro-static
3	general	ellipse	A-s	0.01	hydro-static
4	general	ellipse	A-st	10	elastic shear
5	general	ellipse	a-st	1250	viscous shear

Table 3: Cell budding: different physical test cases considered.

the five different physical test cases shown in Tab. 3 and discussed in the following:

Case 1: The deformation is constrained to remain axisymmetric (the FE nodes are only allowed to move in radial direction⁵). The resulting deformation for $\bar{H}_0 = -25$ is shown in Fig. 12 and in the supplemental movie file `bud1.mpg`.

Case 2: The deformation is not constrained. Consequently, the non-axisymmetric bud shape shown in Fig. 13 appears. Viewed from the top, the bud takes the shape of a ‘+’. Essentially, the initially circular region, where H_0 is prescribed, tries to flow away in order to lower the elastic energy. The flow leads to large mesh distortions and consequently the simulation crashes at $\bar{H}_0 = -23.17$. It is reasonable to suspect that the ‘+’ shape is a consequence of the particular discretization. To confirm this, the following case is considered:

⁵For the given mesh, this does not enforce axisymmetry exactly as a close inspection of the results shows.

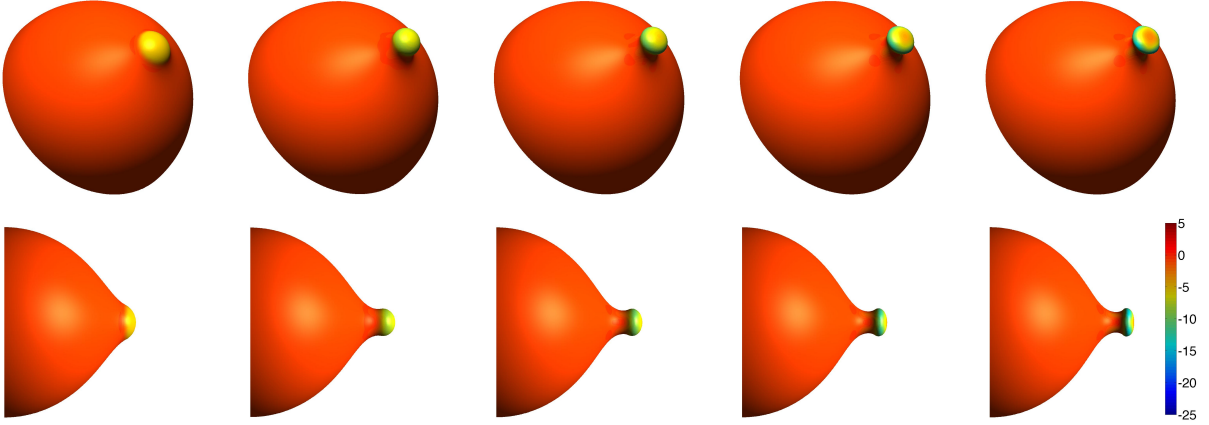


Figure 12: Cell budding: Axisymmetric case at $\bar{H}_0 = -5, -10, -15, -20, -25$ (left to right): 3D and side view of deformation and curvature \bar{H} . Here $\bar{H} \in [-15.0, 0.31]$.

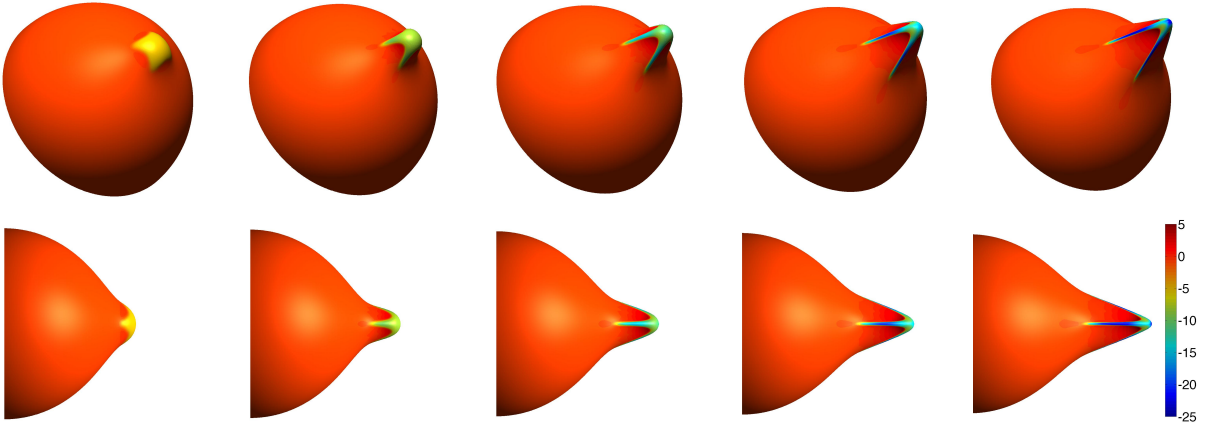


Figure 13: Cell budding: Unconstrained, perfect case at $\bar{H}_0 = -5, -10, -15, -20, -23.17$ (left to right): 3D and side view of deformation and curvature \bar{H} . Here $\bar{H} \in [-24.5, 6.12]$.

Case 3: Instead of a circle, H_0 is prescribed within an imperfect circle, i.e. an ellipse with half-axes $a = 0.22R$ and $b = 0.18R$. The bud now flows into a ‘-’ shape, as is shown in Fig. 14. The distortion of the mesh seen on the right clearly shows how the material flows outward in horizontal direction and back inward in vertical direction. The mesh distortion becomes so large that the simulation crashes at $\bar{H}_0 = -11.98$. In the current case the flow is not resisted mechanically (since μ is so low). Resistance is provided either by shear stiffness (e.g. due to an underlying cytoskeleton) or by viscosity. This is considered in the remaining two cases.

Case 4: Fig. 15 shows the deformation for the same case as before ($a = 0.22R$ and $b = 0.18R$) considering now a shear resisting membrane. Model ‘A-st’⁶ is now considered with $\bar{\mu} = 10$. The shear resistance prevents the unbounded spreading of the bud observed earlier. Now the bud remains localized in the center. The bud starts growing in an almost circular fashion, but then degenerates into the shape shown in Fig. 15. The process suggests that the initial imperfection is only a trigger for the final shape, but does not affect it in magnitude. The evolving deformation for case 4 is also shown in the supplemental movie file `bud4.mpg`.

Case 5: The final case also considers the imperfect circle from before ($a = 0.22R$ and $b =$

⁶The shear stresses are now physical and need to be applied both in-plane and out-of-plane.

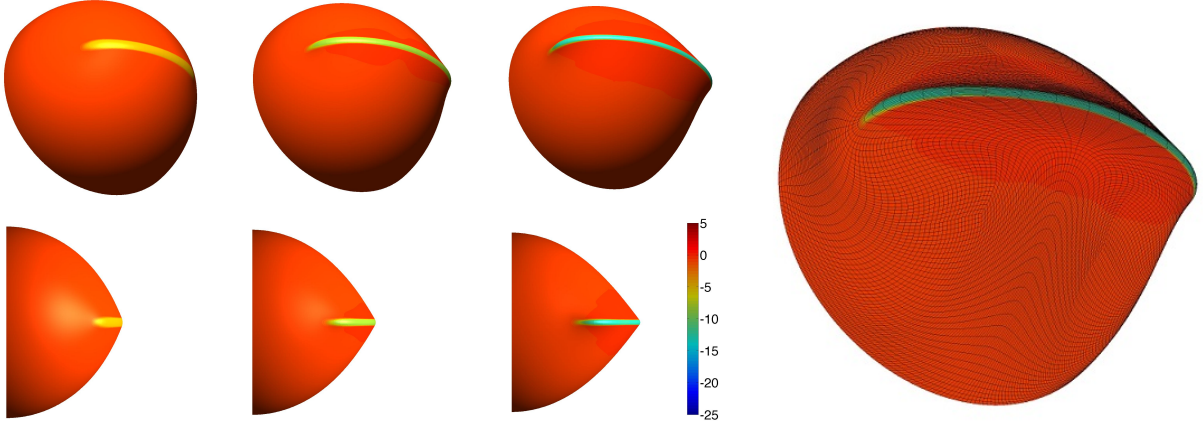


Figure 14: Cell budding: Unconstrained, imperfect case at $\bar{H}_0 = -4, -8, -11.98$ (left to right): 3D and side view of deformation and curvature \bar{H} . Here $\bar{H} \in [-12.5, -0.27]$.

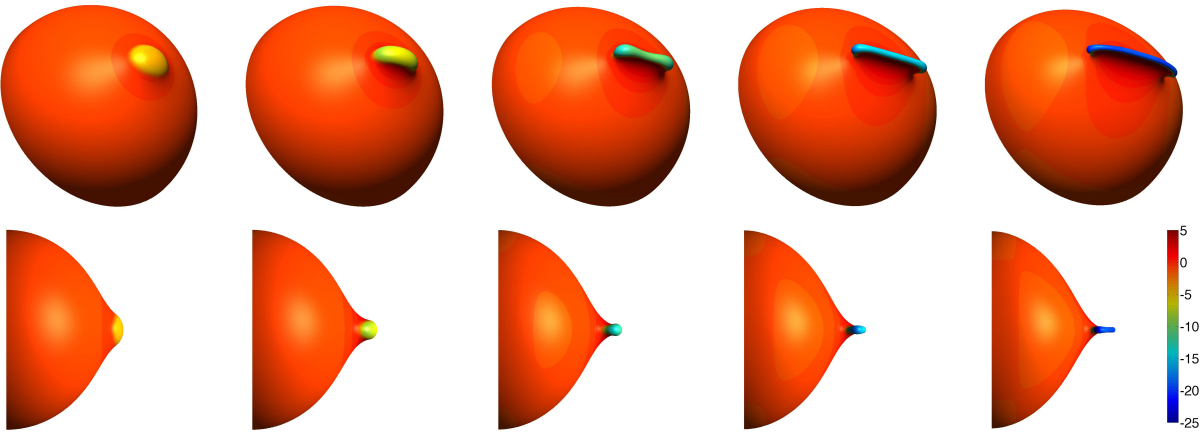


Figure 15: Cell budding: Shear resistant, imperfect case at $\bar{H}_0 = -5, -10, -15, -20, -25$ (left to right): 3D and side view of deformation and curvature \bar{H} . Here $\bar{H} \in [-22.8, 4.61]$.

$0.18R$), but now provides significant shear stress through physical viscosity. This is captured through model ‘a-st’ using relation (56) with $\bar{\mu} = 1250$ and a load stepping increment for H_0 of $\Delta\bar{H}_0 = 0.02$ (such that $\nu = 25k/L^3/\dot{H}_0$, where \dot{H}_0 is the rate with which the spontaneous curvature is prescribed). The evolution of the bud with H_0 is shown in Fig. 16 and in the supplemental movie file `bud5.mpg`. Again, the bud starts growing in an almost circular fashion, but then degenerates into a plate-like shape. If H_0 is kept fixed over time, the solution of case 5 will relax to the solution of case 3.

5.4.4 Surface energy

By examining the surface energy

$$\Pi := \int_{S_0} W \, dA, \quad (104)$$

it can be seen that the non-axisymmetric shapes are preferred. As Fig. 17 shows case 2 and 3 have much lower surface energy than case 1. The difference becomes especially large below $H_0 = 4/R$, when the deformations become large. As the system tries to minimize energy, this

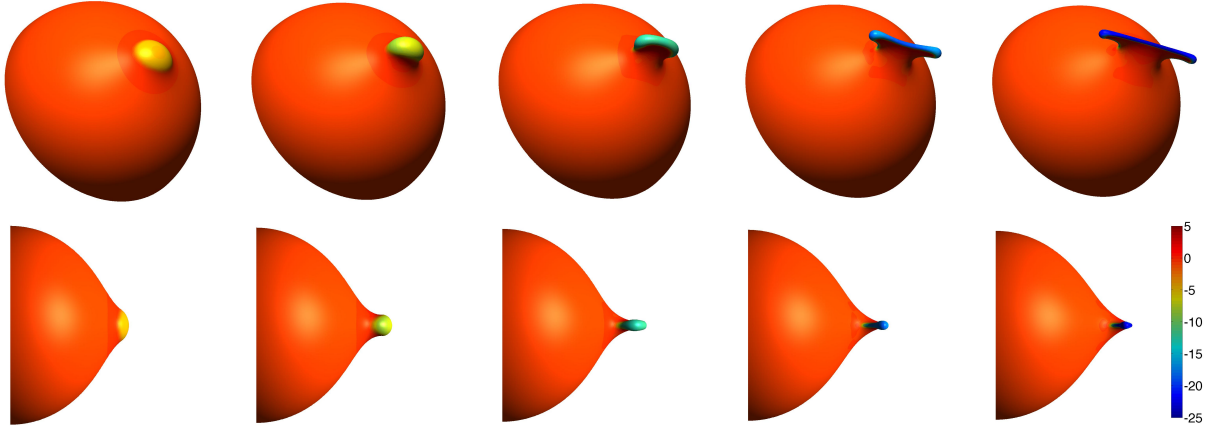


Figure 16: Cell budding: Viscous, imperfect case at $\bar{H}_0 = -5, -10, -15, -20, -25$ (left to right): 3D and side view of deformation and curvature \bar{H} . Here $\bar{H} \in [-24.4, 4.29]$.

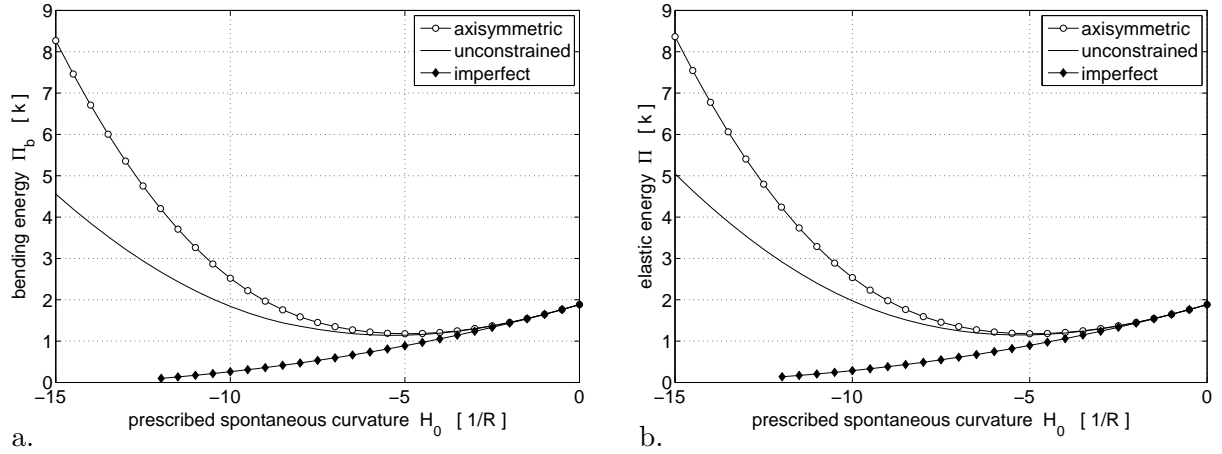


Figure 17: Cell budding: elastic surface energy vs. spontaneous curvature for the three cases shown in Figs. 12, 13 and 14: a. bending energy; b. total energy (bending + areal part).

shows that the axisymmetric bud shape of case 1 is not a preferred solution. As the figure shows, almost all of the energy goes into bending (contribution Jw in (27)), as the areal part (contribution $Kg^2/2$ in (27)) becomes negligible for near incompressibility.

5.4.5 Surface tension

One of the advantages of the proposed finite element formulation is that the surface tension γ can be studied. This is done here for cases 1, 4 and 5 listed above. It was shown before that the surface tension is not uniform under protein-induced spontaneous curvature through FE simulations utilizing Monge patches (Rangamani et al., 2014). The current simulations confirm this result and in addition yield further understanding for large deformations.

First, the axisymmetric case (case 1) is examined in Fig. 18. As seen γ becomes maximum within the protein patch. This maximum is constant across the patch for low H_0 . This changes for increasing H_0 , where a distinct maximum appears in the center.⁷ At a certain level of H_0

⁷It can be seen that the distribution of γ is not exactly axisymmetric. This is due to the inexact enforcement

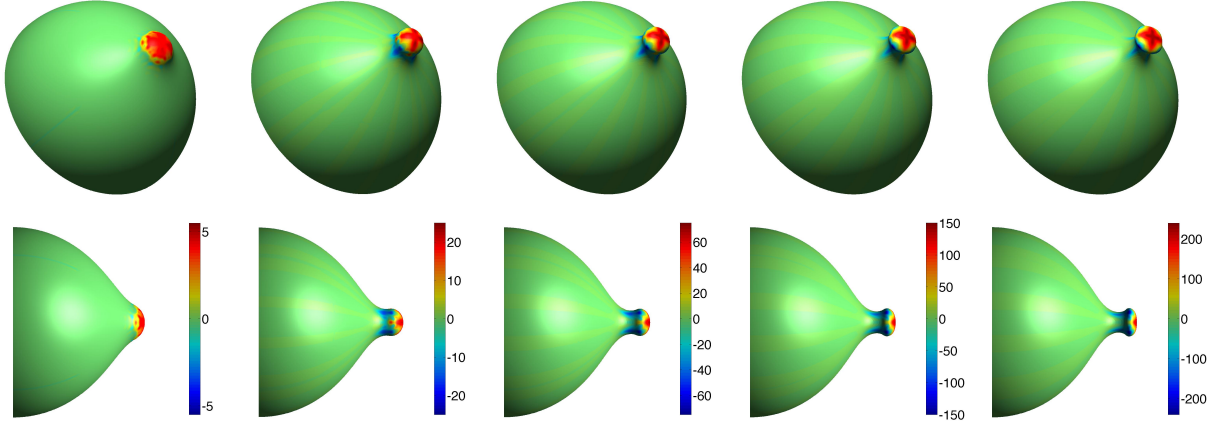


Figure 18: Cell budding: Axisymmetric case at $\bar{H}_0 = -5, -10, -15, -20, -25$ (left to right): 3D and side view of deformation and surface tension $\bar{\gamma}$.

rupture would occur here, depending on the strength of the lipid bilayer.

Second, the shear stiff case (case 4) is examined in Fig. 19. As the plate-like bud appears, the

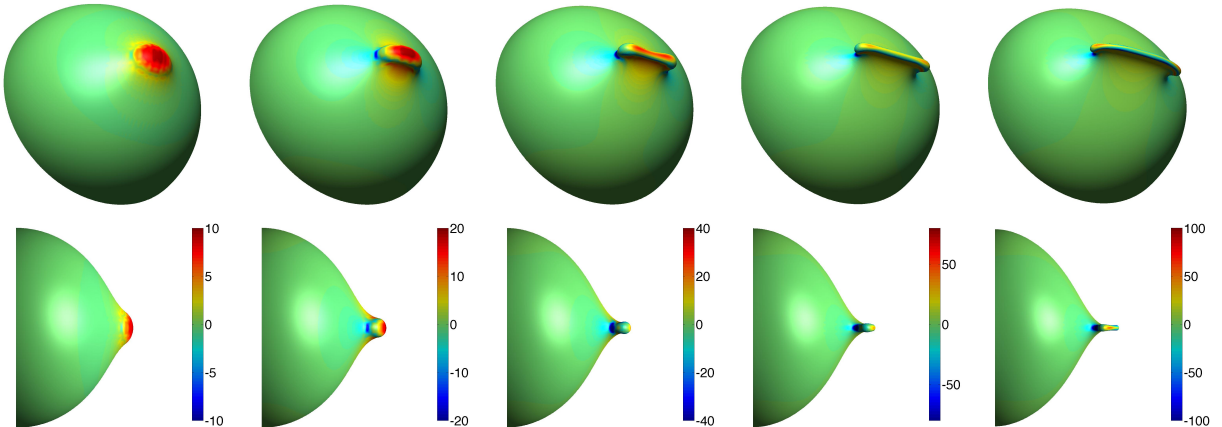


Figure 19: Cell budding: Shear resistant, imperfect case at $\bar{H}_0 = -5, -10, -15, -20, -25$ (left to right): 3D and side view of deformation and surface tension $\bar{\gamma}$.

maximum of γ moves away from the center and is concentrated at the end of the plate. The behavior is similar for the viscous case (case 5) shown in Fig. 20. Both case 4 and 5 show that the extrema of γ are concentrated in very small regions associated with large curvatures. However, these peak values are still much lower than the more distributed peak values of case 1. The lower values are not surprising, as the system has much lower energy for non-axisymmetric shapes. For the non-axisymmetric cases with shear stiffness (case 4) and viscosity (case 5), the resulting surface tensions are of similar magnitude. Only the shapes are different.

5.4.6 Effective shear stiffness

Fig. 21 shows the sign of the effective shear stiffness μ_{eff} for cases 1 and 4.⁸ It can be seen that for of axisymmetry noted in footnote 4.

⁸For case 4, the physical shear stiffness $\bar{\mu} = 10$ needs to be added to Eq. (39).

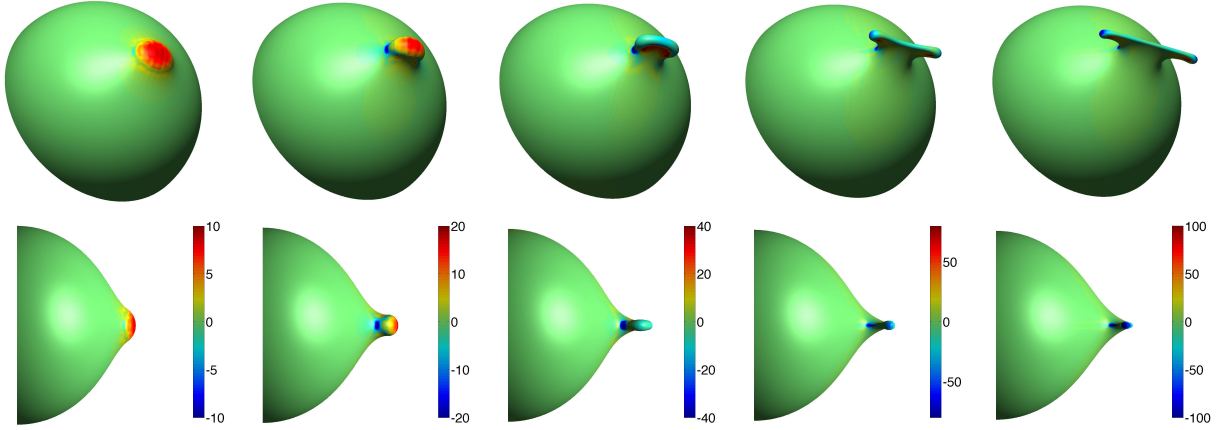


Figure 20: Cell budding: Viscous, imperfect case at $\bar{H}_0 = -5, -10, -15, -20, -25$ (left to right): 3D and side view of deformation and surface tension $\bar{\gamma}$.

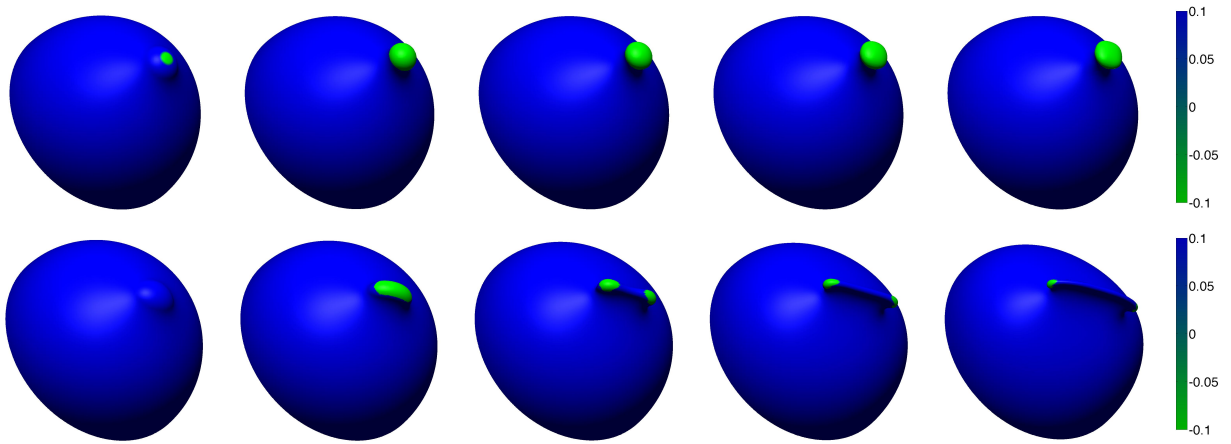


Figure 21: Cell budding: sign of $\bar{\mu}_{\text{eff}}$ for cases 1 (top) and 4 (bottom) at $\bar{H}_0 = -5, -10, -15, -20, -25$ (left to right).

both cases, μ_{eff} is negative in some regions. The minimum values of $\bar{\mu}_{\text{eff}}$ reaches down to -150 in case 1 and to -50 in case 4. Since the simulations run stably, even though $\mu_{\text{eff}} < 0$, there must be another stabilizing effect. It is probable that this related to the geometry: The figure shows that the regions of negative μ_{eff} are all convex. The condition $\mu_{\text{eff}} < 0$ is therefore not sufficient for unstable behavior. Since stabilization may be provided naturally, the computations can sometimes be performed with no stabilization scheme. In practice it is however recommended to add one of the stabilization schemes proposed in Sec. 3. For example, when both H and κ are zero neither the Helfrich model nor the geometry can be expected to stabilize the structure. The stabilization parameters (μ and n_t) can be picked such that the stabilization scheme does not affect the physical behavior. This is the case for the stabilization chosen here.

5.4.7 Influence of the area-compressibility

As a final study, we investigate the influence of the area-compressibility (parameter K) and compare the behavior of model (27), that depends on K , with (29), where K is infinite. For this purpose, model (29) is discretized according to Sec. 4.3. In theory, the behavior of model

(27), should approach that of model (29) as $K \rightarrow \infty$.

For case 1, there is no significant difference between the two models as Fig. 22 shows. Only

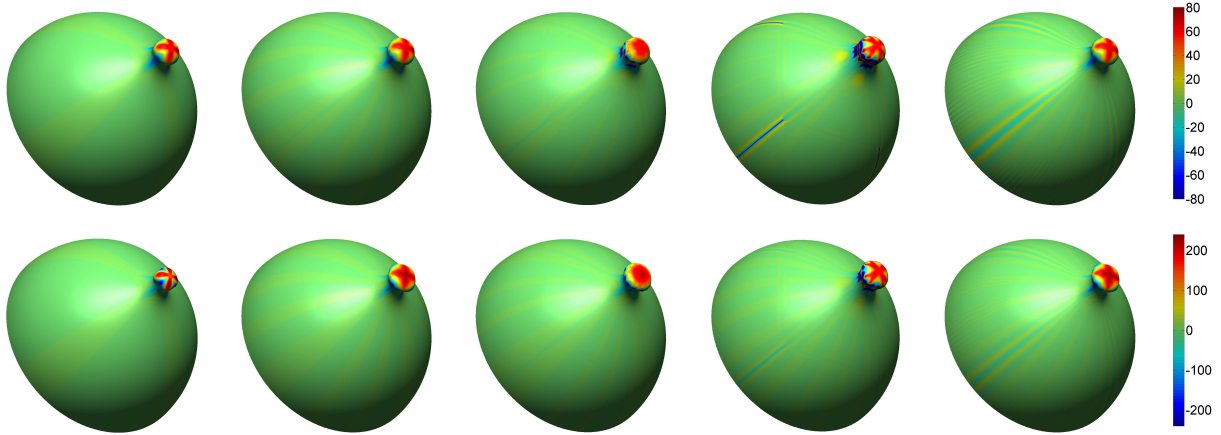


Figure 22: Cell budding: influence of K for the axisymmetric case (case 1) for $\bar{H}_0 = -15$ (top) and $\bar{H}_0 = -25$ (bottom) considering $\bar{K} = 10^3, 10^4, 10^5, 10^6, \infty$ (left to right). The color shows $\bar{\gamma}$.

for the lowest K , differences appear. Between all other cases, the bud shape only changes minimally. However, increasing K in formulation (27) leads to oscillations in γ .

For case 5, a strong dependency on K appears, as Fig. 23 shows. Now, the deformation clearly

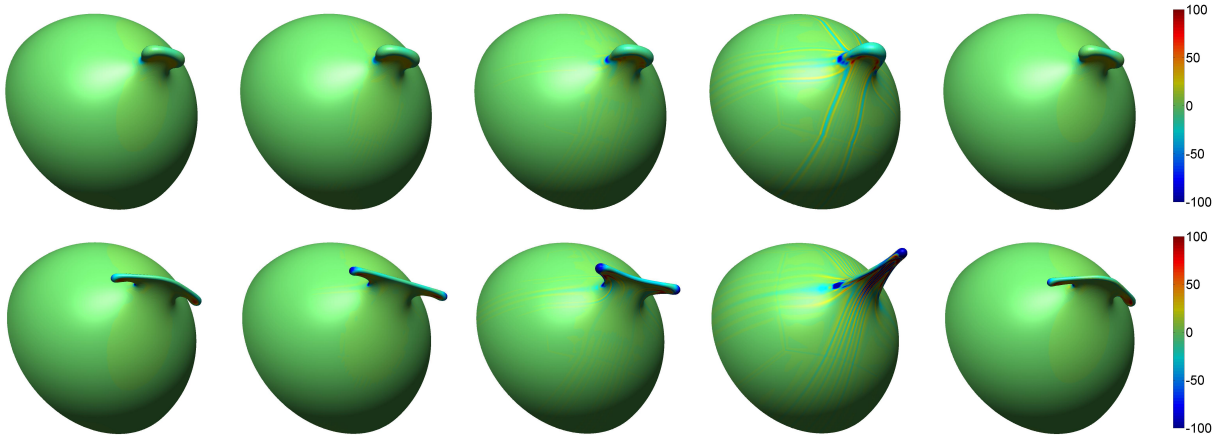


Figure 23: Cell budding: influence of K for the viscous case (case 5) for $\bar{H}_0 = -15$ (top) and $\bar{H}_0 = -25$ (bottom) considering $\bar{K} = 10^3, 10^4, 10^5, 10^6, \infty$ (left to right). The color shows $\bar{\gamma}$.

does not converge with increasing K in (27). Instead, the solution for $\bar{K} = 10^3$ is closest to the solution from model (29). The figure also shows that oscillations appear in the solution from model (27) as K increases. Essentially, the problem of model (27) is that even though J converges to 1, as Fig. 24 shows, the pressure q does not converge. This can be seen in Fig. 25 for the pure bending problem of Sec. 5.1, which has an analytical solution for q . As the figure shows, there is an optimal value of K , where the pressure error is minimal and beyond which it diverges. This is different to examples in computational contact mechanics, where both kinematic and kinetic variables can converge with increasing penalty parameter (Sauer and De Lorenzis, 2015). So even though model (27) is simpler and more efficient, it has to be used

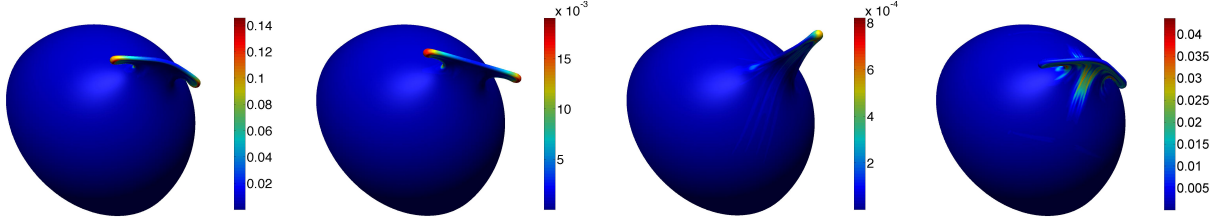


Figure 24: Cell budding: influence of K for case 5 for $\bar{H}_0 = -25$ considering $\bar{K} = 10^3, 10^4, 10^6, \infty$ (left to right). The color shows the relative error in J given by $|J - 1|$.

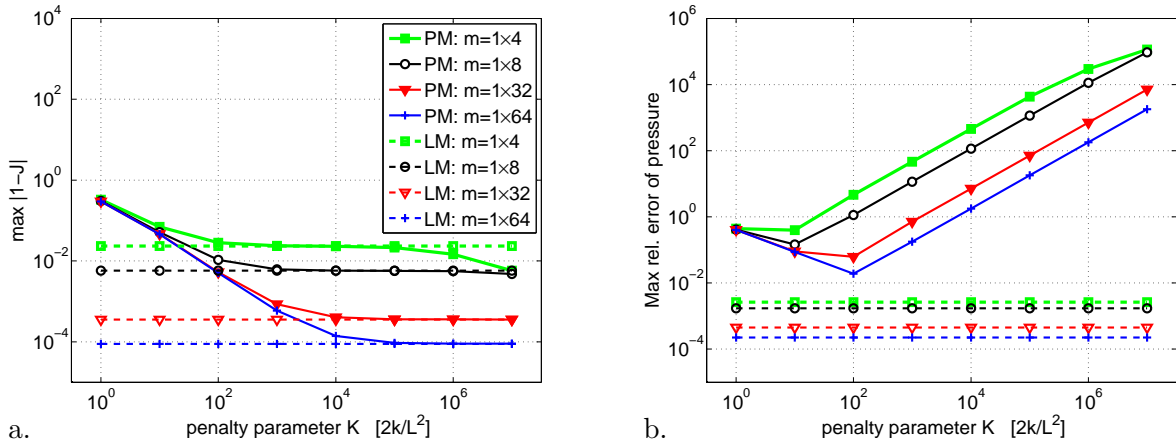


Figure 25: Pure bending: accuracy of the penalty regularization (27) compared to the Lagrange multiplier formulation (29): a. error in stretch J ; b. error in pressure q . As seen, J can be more accurate, while q does not converge with K . There is rather an optimum K that minimizes the pressure error.

with care, as the solution can become wrong. If an implementation of (29) is not available, the mesh convergence of model (27) should be examined

6 Conclusion

This paper presents a general computational formulation for lipid bilayers based on general thin-shell kinematics, the Helfrich bending model, and 3D, LBB-conforming, C^1 -continuous NURBS-based finite elements. The rotational continuity of the formulation is ensured by using a rotational constraint across the patch boundaries in the FE mesh. Two cases are considered in order to model the in-plane membrane response: area-compressibility and area-incompressibility, and for both suitable FE formulations are presented. Since the formulation lacks shear stiffness, several shear stabilization schemes are proposed for quasi-static computations. They are based on adding either numerical stiffness (class **A**), numerical viscosity (class **a**) or performing a projection of the solution onto the shell manifold (class **P**). The numerical viscosity scheme can also be used to model physical viscosity as the example in Fig. 16 illustrates, while the numerical stiffness scheme can also be used to model physical stiffness as the example in Fig. 15 illustrates. It is further shown that the Helfrich bending model provides intrinsic shear stiffness as long as the surface curvature is non-zero. Altogether, four different computational examples are considered in order to verify the formulation and to study its physical behavior. The last ex-

ample shows that the 3D budding behavior of lipid bilayers – as described by the Helfrich model – can become very complex, even though the model is purely mechanical and does not account for other effects, such as diffusion or temperature. Computational challenges arise especially for area-incompressible, non-axisymmetric bilayer shapes. For these a penalty regularization can give misleading results.

The paper shows that the proposed computational model is not only capable of capturing complex deformations, but is also a suitable tool to analyse and understand the stresses and energetics of lipid bilayers. Still, more work is needed in order to further advance the computational modeling of lipid bilayers. For example, the modeling of surface flow, protein diffusion, multicomponent lipids and thermal fluctuations would be useful extensions of the present work.

Acknowledgements

The authors are grateful to the German Research Foundation (DFG) for supporting this research under grants GSC 111 and SA1822/5-1. They acknowledge support from the University of California at Berkeley and from Director, Office of Science, Office of Basic Energy Sciences, Chemical Sciences Division, of the U.S. Department of Energy under contract No. DE AC02-05CH11231. Further, they thank the graduate student Yannick Omar for checking the theory.

A Linearization of $\mathbf{f}_{\text{into}}^e$

Alternatively to Eq. (69.2), $\mathbf{f}_{\text{into}}^e$ can be also written as

$$\mathbf{f}_{\text{into}}^e = - \int_{\Omega_0^e} \tau^{\alpha\beta} \mathbf{N}^T (\mathbf{n} \otimes \mathbf{n}) \mathbf{N}_{,\alpha\beta} dA \mathbf{x}_e . \quad (105)$$

The linearization of $\mathbf{f}_{\text{into}}^e$ thus becomes

$$\mathbf{f}_{\text{into}}^e(\mathbf{x}_e + \Delta\mathbf{x}_e) \approx \mathbf{f}_{\text{into}}^e(\mathbf{x}_e) + \Delta\mathbf{f}_{\text{into}}^e , \quad (106)$$

with

$$\begin{aligned} \Delta\mathbf{f}_{\text{into}}^e = & - \int_{\Omega_0^e} \tau^{\alpha\beta} \mathbf{N}^T (\mathbf{n} \otimes \mathbf{n}) \mathbf{N}_{,\alpha\beta} dA \Delta\mathbf{x}_e - \int_{\Omega_0^e} \Delta\tau^{\alpha\beta} b_{\alpha\beta} \mathbf{N}^T \mathbf{n} dA \\ & - \int_{\Omega_0^e} \tau^{\alpha\beta} \mathbf{N}^T (\mathbf{n} \otimes \Delta\mathbf{n}) \mathbf{a}_{\alpha,\beta} dA - \int_{\Omega_0^e} \tau^{\alpha\beta} b_{\alpha\beta} \mathbf{N}^T \Delta\mathbf{n} dA . \end{aligned} \quad (107)$$

Inserting

$$\Delta\tau^{\alpha\beta} = c^{\alpha\beta\gamma\delta} \mathbf{a}_\gamma \cdot \mathbf{N}_{,\delta} \Delta\mathbf{x}_e \quad (108)$$

(Sauer et al., 2014) and

$$\Delta\mathbf{n} = -\mathbf{a}^\gamma (\mathbf{n} \cdot \Delta\mathbf{a}_\gamma) \quad (109)$$

(Wriggers, 2006), we get

$$\Delta\mathbf{f}_{\text{into}}^e = \mathbf{k}_{\text{into}}^e \Delta\mathbf{x}_e , \quad (110)$$

with the tangent matrix

$$\begin{aligned} \mathbf{k}_{\text{into}}^e = & - \int_{\Omega_0^e} \tau^{\alpha\beta} \mathbf{N}^T (\mathbf{n} \otimes \mathbf{n}) \mathbf{N}_{,\alpha\beta} dA - \int_{\Omega_0^e} c^{\alpha\beta\gamma\delta} b_{\alpha\beta} \mathbf{N}^T (\mathbf{n} \otimes \mathbf{a}_\gamma) \mathbf{N}_{,\delta} dA \\ & + \int_{\Omega_0^e} \tau^{\alpha\beta} \Gamma_{\alpha\beta}^\gamma \mathbf{N}^T (\mathbf{n} \otimes \mathbf{n}) \mathbf{N}_{,\gamma} dA + \int_{\Omega_0^e} \tau^{\alpha\beta} b_{\alpha\beta} \mathbf{N}^T (\mathbf{a}^\gamma \otimes \mathbf{n}) \mathbf{N}_{,\gamma} dA . \end{aligned} \quad (111)$$

Here, $\Gamma_{\alpha\beta}^\gamma := \mathbf{a}^\gamma \cdot \mathbf{a}_{\alpha,\beta}$ defines the Christoffel symbol of the second kind. The tensor components $c^{\alpha\beta\gamma\delta}$ are given in [Sauer and Duong \(2015\)](#) for various material models. For an efficient implementation, the contractions appearing above should be worked out analytically.

B Linearization of \mathbf{g}^e

The vector \mathbf{g}^e is independent of the Lagrange multiplier and thus only depends on \mathbf{x}_e . The linearization of \mathbf{g}^e thus is

$$\mathbf{g}^e(\mathbf{x}_e + \Delta\mathbf{x}_e) \approx \mathbf{g}^e(\mathbf{x}_e) + \Delta\mathbf{g}^e, \quad (112)$$

with

$$\Delta\mathbf{g}^e = \int_{\Omega_0^e} \mathbf{L}^T \Delta g \, dA, \quad (113)$$

and ([Sauer and Duong, 2015](#))

$$\Delta g = \Delta J = \frac{J}{2} a^{\alpha\beta} \Delta a_{\alpha\beta}. \quad (114)$$

Inserting the discretisation of $\Delta a_{\alpha\beta}$ ([Duong et al., 2015](#)), and exploiting the symmetry of $a^{\alpha\beta}$, we get the approximation

$$\Delta g \approx J \mathbf{a}^\alpha \cdot \mathbf{N}_{,\alpha} \Delta \mathbf{x}_e, \quad (115)$$

such that

$$\Delta \mathbf{g}^e = \mathbf{k}_g^e \Delta \mathbf{x}_e, \quad (116)$$

with the tangent matrix

$$\mathbf{k}_g^e := \int_{\Omega_0^e} \mathbf{L}^T \mathbf{a}^\alpha \cdot \mathbf{N}_{,\alpha} J \, dA. \quad (117)$$

References

- Agrawal, A. and Steigmann, D. (2009). Modeling protein-mediated morphology in biomembranes. *Biomech. Model. Mechanobiol.*, **8**(5):371–379.
- Aris, R. (1989). *Vectors, tensors and the basic equations of fluid mechanics*. Dover, Mineola.
- Arroyo, M. and DeSimone, A. (2009). Relaxation dynamics of fluid membranes. *Phys. Rev. E*, **79**:031915.
- Babuška, I. (1973). The finite element method with Lagrangian multipliers. *Num. Math.*, **20**:179–192.
- Baesu, E., Rudd, R. E., Belak, J., and McElfresh, M. (2004). Continuum modeling of cell membranes. *Int. J. Non-lin. Mech.*, **39**:369–377.
- Bathe, K.-J. (1996). *Finite Element Procedures*. Prentice-Hall, New Jersey.
- Borden, M. J., Scott, M. A., Evans, J. A., and Hughes, T. J. R. (2011). Isogeometric finite element data structures based on Bezier extraction of NURBS. *Int. J. Numer. Meth. Engng.*, **87**:15–47.
- Budin, I., Bruckner, R. J., and Szostak, J. W. (2009). Formation of protocell-like vesicles in a thermal diffusion column. *Journal of the American Chemical Society*, **131**(28):9628–9629.

- Buser, C. and Drubin, D. G. (2013). Ultrastructural imaging of endocytic sites in *Saccharomyces cerevisiae* by transmission electron microscopy and immunolabeling. *Microscopy and Microanalysis*, **19**(02):381–392.
- Canham, P. B. (1970). The minimum energy of bending as a possible explanation of the biconcave shape of the human red blood cell. *J. Theoret. Biol.*, **26**:61–81.
- Cirak, F. and Ortiz, M. (2001). Fully C^1 -conforming subdivision elements for finite element-deformation thin-shell analysis. *Int. J. Numer. Meth. Engng*, **51**:813–833.
- Cottrell, J. A., Hughes, T. J. R., and Bazilevs, Y. (2009). *Isogeometric Analysis*. Wiley.
- Dao, M., Lim, C. T., and Suresh, S. (2003). Mechanics of the human red blood cell deformed by optical tweezers. *J. Mech. Phys. Solids*, **51**:2259–2280.
- Derényi, I., Jülicher, F., and Prost, J. (2002). Formation and interaction of membrane tubes. *Phy. Rev. Lett.*, **88**(23):238101.
- Du, Q. and Wang, X. Q. (2007). Convergence of numerical approximations to a phase field bending elasticity model of membrane deformations. *Int. J. Numer. Anal. Model.*, **4**(3-4):441–459.
- Duong, T. X., Roohbakhshan, F., and Sauer, R. A. (2015). A new rotation-free isogeometric thin shell formulation and a corresponding continuity constraint for patch boundaries. *submitted*, (see supplemental material).
- Elliott, C. M. and Stinner, B. (2010). Modeling and computation of two phase geometric biomembranes using surface finite elements. *J. Comp. Phys.*, **229**(18):6585–6612.
- Fawcett, D. W. (1981). *The Cell*. Saunders, Philadelphia.
- Feng, F. and Klug, W. S. (2006). Finite element modeling of lipid bilayer membranes. *J. Comput. Phys.*, **220**:394–408.
- Griparic, L. and van der Blik, A. M. (2001). The many shapes of mitochondrial membranes. *Traffic*, **2**(4):235–244.
- Gruenberg, J. and Stenmark, H. (2004). The biogenesis of multivesicular endosomes. *Nature Reviews Molecular Cell Biology*, **5**(4):317–323.
- Gu, R., Wang, X., and Gunzburger, M. (2014). Simulating vesicle-substrate adhesion using two phase field functions. *J. Comp. Phys.*, **275**:626–641.
- Helfrich, W. (1973). Elastic properties of lipid bilayers: Theory and possible experiments. *Z. Naturforsch.*, **28c**:693–703.
- Hu, J., Shibata, Y., Zhu, P.-P., Voss, C., Rismanchi, N., Prinz, W. A., Rapoport, T. A., and Blackstone, C. (2009). A class of dynamin-like gtpases involved in the generation of the tubular er network. *Cell*, **138**(3):549–561.
- Itoh, T., Erdmann, K. S., Roux, A., Habermann, B., Werner, H., and De Camilli, P. (2005). Dynamin and the actin cytoskeleton cooperatively regulate plasma membrane invagination by bar and f-bar proteins. *Developmental cell*, **9**(6):791–804.
- Jarić, M., Seifert, U., Wirtz, W., and Wortis, M. (1995). Vesicular instabilities: The prolate-to-oblate transition and other shape instabilities of fluid bilayer membranes. *Phys. Rev. E*, **52**(6):6623–6634.

- Jie, Y., Quanhui, L., Jixing, L., and Zhong-Can, O.-Y. (1998). Numerical observation of non-axisymmetric vesicles in fluid membranes. *Phys. Rev. E*, **58**(4):4730–4736.
- Kahraman, O., Stoop, N., and Müller, M. M. (2012). Fluid membrane vesicles in confinement. *New J. Phys.*, **14**:095021.
- Karotki, L., Huiskonen, J. T., Stefanand, C. J., Ziólkowska, N. E., Roth, R., Surma, M. A., Krogan, N. J., Emr, S. D., Heuser, J., Grünewald, K., and Walther, T. C. (2011). Eisosome proteins assemble into a membrane scaffold. *J. Cell Biol.*, **195**(5):889–902.
- Keren, K. (2011). Cell motility: the integrating role of the plasma membrane. *European Biophysics Journal*, **40**(9):1013–1027.
- Kishimoto, T., Sun, Y., Buser, C., Liu, J., Michelot, A., and Drubin, D. G. (2011). Determinants of endocytic membrane geometry, stability, and scission. *Proc. Natl. Acad. Sci.*, **108**:E979–988.
- Kloppel, T. and Wall, W. A. (2011). A novel two-layer, coupled finite element approach for modeling the nonlinear elastic and viscoelastic behavior of human erythrocytes. *Biomech. Model. Mechanobiol.*, **10**(4):445–459.
- Koster, G., VanDuijn, M., Hofs, B., and Dogterom, M. (2003). Membrane tube formation from giant vesicles by dynamic association of motor proteins. *Proceedings of the National Academy of Sciences*, **100**(26):15583–15588.
- Kozlov, M. M., Campelo, F., Liska, N., Chernomordik, L. V., Marrink, S. J., and McMahon, H. T. (2014). Mechanisms shaping cell membranes. *Current opinion in cell biology*, **29**:53–60.
- Kukulski, W., Schorb, M., Kaksonen, M., and Briggs, J. A. G. (2012). Plasma membrane reshaping during endocytosis is revealed by time-resolved electron tomography. *Cell*, **150**(3):508–520.
- Lau, C., Brownell, W. E., and Spector, A. A. (2012). Internal forces, tension and energy density in tethered cellular membranes. *J. Biomech.*, **45**(7):1328–1331.
- Li, H. and Lykotrafitis, G. (2012). Two-component coarse-grained molecular-dynamics model for the human erythrocyte membrane. *Biophys. J.*, **102**(1):75–84.
- Ma, L. and Klug, W. S. (2008). Viscous regularization and r-adaptive meshing for finite element analysis of lipid membrane mechanics. *J. Comput. Phys.*, **227**:5816–5835.
- McMahon, H. T. and Gallop, J. L. (2005). Membrane curvature and mechanisms of dynamic cell membrane remodelling. *Nature*, **438**(7068):590–596.
- Peng, Z., Asaro, R. J., and Zhu, Q. (2010). Multiscale simulation of erythrocyte membranes. *Phys. Rev. E*, **81**:031904.
- Peter, B. J., Kent, H. M., Mills, I. G., Vallis, Y., Butler, P. J. G., Evans, P. R., and McMahon, H. T. (2004). Bar domains as sensors of membrane curvature: the amphiphysin bar structure. *Science*, **303**(5657):495–499.
- Rahimi, M. and Arroyo, M. (2012). Shape dynamics, lipid hydrodynamics, and the complex viscoelasticity of bilayer membranes. *Phys. Rev. E*, **86**:011932.
- Ramakrishnan, N., Kumar, P. B. S., and Ipsen, J. H. (2010). Monte carlo simulations of fluid vesicles with in-plane orientational ordering. *Phys. Rev. E*, **81**:041922.

- Rangamani, P., Agrawal, A., Mandadapu, K. K., Oster, G., and Steigmann, D. J. (2013). Interaction between surface shape and intra-surface viscous flow on lipid membranes. *Biomech. Model. Mechanobiol.*, **12**(4):833–845.
- Rangamani, P., Mandadapu, K. K., and Oster, G. (2014). Protein-induced membrane curvature alters local membrane tension. *Biophysical journal*, **107**(3):751–762.
- Rangarajan, R. and Gao, H. (2015). A finite element method to compute three-dimensional equilibrium configurations of fluid membranes: Optimal parameterization, variational formulation and applications. *J. Comp. Phys.*, **297**:266–294.
- Rim, J. E., Purohit, P. K., and Klug, W. S. (2014). Mechanical collapse of confined fluid membrane vesicles. *Biomech. Model. Mechanobiol.*, **13**(6):1277–1288.
- Rosolen, A., Peco, C., and Arroyo, M. (2013). An adaptive meshfree method for phase-field models of biomembranes. Part I: Approximation with maximum-entropy basis functions. *J. Comput. Phys.*, **249**:303–319.
- Salac, D. and Miksis, M. (2011). A level set projection model of lipid vesicles in general flows. *J. Comput. Phys.*, **230**(22):8192–8215.
- Sauer, R. A. (2014). Stabilized finite element formulations for liquid membranes and their application to droplet contact. *Int. J. Numer. Meth. Fluids*, **75**(7):519–545.
- Sauer, R. A. and De Lorenzis, L. (2015). An unbiased computational contact formulation for 3D friction. *Int. J. Numer. Meth. Engrg.*, **101**(4):251–280.
- Sauer, R. A. and Duong, T. X. (2015). On the theoretical foundations of solid and liquid shells. *Math. Mech. Solids*, published online, DOI: 10.1177/1081286515594656.
- Sauer, R. A., Duong, T. X., and Corbett, C. J. (2014). A computational formulation for solid and liquid membranes based on curvilinear coordinates and isogeometric finite elements. *Comput. Methods Appl. Mech. Engrg.*, **271**:48–68.
- Shemesh, T., Klemm, R. W., Romano, F. B., Wang, S., Vaughan, J., Zhuang, X., Tukachinsky, H., Kozlov, M. M., and Rapoport, T. A. (2014). A model for the generation and interconversion of er morphologies. *Proceedings of the National Academy of Sciences*, **111**(49):E5243–E5251.
- Shi, Z. and Baumgart, T. (2015). Membrane tension and peripheral protein density mediate membrane shape transitions. *Nature communications*, **6**:5974.
- Shibata, Y., Hu, J., Kozlov, M. M., and Rapoport, T. A. (2009). Mechanisms shaping the membranes of cellular organelles. *Annual Review of Cell and Developmental Biology*, **25**:329–354.
- Shibata, Y., Voeltz, G. K., and Rapoport, T. A. (2006). Rough sheets and smooth tubules. *Cell*, **126**(3):435–439.
- Steigmann, D. J. (1999). Fluid films with curvature elasticity. *Arch. Rat. Mech. Anal.*, **150**:127–152.
- Tasso, I. V. and Buscaglia, G. C. (2013). A finite element method for viscous membranes. *Comput. Meth. Appl. Mech. Engrg.*, **255**:226–237.
- Terasaki, M., Chen, L. B., and Fujiwara, K. (1986). Microtubules and the endoplasmic reticulum are highly interdependent structures. *The Journal of Cell Biology*, **103**(4):1557–1568.

- Walani, N., Torres, J., and Agrawal, A. (2015). Endocytic proteins drive vesicle growth via instability in high membrane tension environment. *Proceedings of the National Academy of Sciences*, **112**(12):E1423–E1432.
- Walther, T. C., Brickner, J. H., Aguilera, P. S., Bernales, S., Pantoja, C., and Walter, P. (2006). Eisosomes mark static sites of endocytosis. *Nature*, **439**:998–1003.
- Waterman-Storer, C. M. and Salmon, E. D. (1998). Endoplasmic reticulum membrane tubules are distributed by microtubules in living cells using three distinct mechanisms. *Current Biology*, **8**(14):798–807.
- Wriggers, P. (2006). *Computational Contact Mechanics*. Springer, 2nd edition.
- Wriggers, P. (2008). *Nonlinear Finite Element Methods*. Springer.
- Zimmerberg, J. and Kozlov, M. M. (2006). How proteins produce cellular membrane curvature. *Nature Reviews Molecular Cell Biology*, **7**(1):9–19.